Dynamic persistence of intracellular bacterial communities of uropathogenic Escherichia coli in a human bladder-chip model of urinary tract infections

Authors: Kunal Sharma, Neeraj Dhar*[&], Vivek V. Thacker*[&], Thomas Simonet, François Signorino-Gelo, Graham Knott, John D. McKinney*

Affiliations:

School of Life Sciences, Swiss Federal Institute of Technology in Lausanne (EPFL), 1015 Lausanne, Switzerland.

[&] These authors corresponded equally

*Correspondence to: neeraj.dhar@epfl.ch, vivekvthacker@gmail.com , john.mckinney@epfl.ch

Abstract

Uropathogenic *Escherichia coli* (UPEC) is the most common causative agent of urinary tract infections and is a major cause for antibiotic prescriptions. Previous studies have shown that infection of terminally differentiated urinary bladder cells leads to the formation of intracellular bacterial communities (IBCs). However, the precise role of IBCs in recurrence of infection and antibiotic persistence, is not completely understood in part because the *in situ* dynamic responses of bacteria within these structures to antibiotic stress is difficult to assess in animal models. Here, we develop and characterize a human bladder-chip model of UPEC infection wherein superficial bladder epithelial cells and bladder microvascular endothelial cells are co-cultured under flow in urine and nutritive media respectively, and the mechanics of bladder filling and voiding cycles mimicked by application and release of linear strain. Time-lapse microscopy showed that infection of epithelial cells under shear stress in diluted urine led to the rapid recruitment and diapedesis of neutrophils across the endothelial-epithelial barrier and the formation of neutrophil swarms and neutrophil extracellular traps. Subsequently, two cycles of antibiotic administration interspersed with recovery periods revealed both non-growing and rapidly proliferating IBCs. Multiple stages of IBC formation captured on-chip with single-cell resolution revealed that that bacterial killing within IBCs was substantially delayed, outcomes such as shedding of bacteria and exfoliation are not mutually exclusive and rapidly reseeded the infection, and in rare instances bacterial growth in IBCs continued for the entire period of antibiotic administration. These new insights into the early stages of pathogenesis revisit the role of IBCs as harbours of persistent bacterial populations, with significant consequences for non-compliance with antibiotic regimens.

Keywords: bladder-chip, uropathogenic *Escherichia coli* (UPEC), intracellular bacterial communities (IBCs), bacterial persistence, antibiotic treatment, neutrophil swarms, neutrophil extracellular traps, shear stress, stretching, confocal live-cell imaging

Introduction

Urinary tract infections (UTIs), the second most-common cause for the prescription of antibiotics (Foxman, 2010) are characterized by the high frequency of recurrence, defined as a reappearance of infection within 12 months despite the apparently successful completion of antibiotic therapy. Recurrence occurs in about 25% of all UTIs (Foxman et al., 2000) and strongly impacts the cost of healthcare and reduces the quality of life, particularly considering the fact that more than 60% of women are diagnosed with a UTI at least once in their lifetime (Klein and Hultgren, 2020). Uropathogenic *Escherichia coli* (UPEC), the causative agent for the majority of UTIs, exhibits a complex lifestyle in the bladder, with planktonic sub-populations within the urine co-existing with intracellular bacteria. UPEC invasion of the urinary bladder generates substantial changes to bladder morphology and a robust immune response. Much of our current understanding of early stages of UTI and the intracellular lifestyle is derived from studies in the mouse model (Anderson et al., 2003; Hannan et al., 2012; Hung et al., 2009; Justice et al., 2004) ,. Examinations of mouse bladder explants via microscopy have revealed the formation of intracellular bacterial communities (IBCs) composed of thousands of bacteria within individual superficial bladder cells (Justice et al., 2004). IBCs also play a prominent role in clinical infection and have also been harvested from the urine of cystitis patients (Robino et al., 2013; Rosen et al., 2007). These structures are considered to have a linear progression from an early stage of colonization by single bacteria to an intermediate stage of biofilm-like communities culminating in the release of bacteria at the late stage. However, long-term imaging of infected animals or of explant-tissue is technically challenging and therefore it has been difficult to capture the dynamic changes that underlie the formation of these structures and their consequences to infection.

A key strength of advanced organotypic models such as organ-on-chip (Benam et al., 2016; Huh et al., 2010a; Jang et al., 2013, 2019; Kim et al., 2016; Novak et al., 2020; Zhou et al., 2016) or organoids (Cakir et al., 2019; Clevers, 2016; Rossi et al., 2018; Sato et al., 2009) is that they increasingly recapitulate the complexity of host physiology. The bladder is a particularly challenging organ to mimic; it has a stratified architecture with well-differentiated cell types; a lumen filled with urine whose composition and chemical properties can vary depending on the physiological state of the individual and is subjected to periodic and large changes in organ volume and surface area (Korkmaz and Rogg, 2007). These features may play important roles in infection, but they have been hitherto hard to capture outside of a whole animal model, where they are present in their entirety and cannot be dissected in a modular manner.

Organotypic models are well-suited to address these outstanding questions. Recently, bladder organoids that mimic the stratified architecture of the urothelium have been used to study infections (Horsley et al., 2018; Smith et al., 2006; Sharma et al., 2020). However, the organoid model suffers from certain shortcomings inherent to the 3-D architecture such as the lack of vasculature, the inability to manipulate the cells mechanically, and the constrained volume of the lumen. In contrast, organ-on-chip models offer a complementary approach that does not suffer from these limitations. Organ-on-chip models have been developed for a number of organs either in isolation or in combination (Novak et al., 2020; Ronaldson-Bouchard and Vunjak-Novakovic, 2018). These systems are being increasingly used to model infectious diseases including viral and bacterial infections of the respiratory tract (Nawroth et al., 2020; Si et al., 2020; Thacker et al., 2020b, 2020a), gut (Jalili-Firoozinezhad et al., 2019; Kim et al., 2016; Shah et al., 2016; Tovaglieri et al., 2019), kidney (Wang et al., 2019), and liver (Kang et al., 2017). However, to

our knowledge, there have been no reports of a bladder-on-chip model. While there have been a few studies that have developed *in vitro* bladder models that recreate the stratified architecture of the bladder epithelium (Horsley et al., 2018; Smith et al., 2006; Suzuki et al., 2019), they have not been used to recapitulate the multiple stages of IBC formation. Similarly, while a few studies have visualized different stages of IBC development by culturing human bladder cells under urine flow, these models are restricted to monoculture experiments(Andersen et al., 2012; Iosifidis and Duggin, 2020). Furthermore, the lack of vasculature in these models restricts the extent to which immune cell components or drugs can be introduced in a physiologically relevant manner and none of the systems reported to date offer the possibility of mimicking bladder mechanics(Andersen et al., 2012; Horsley et al., 2018; Iosifidis and Duggin, 2020; Smith et al., 2006).

Here we report the development and characterization of a bladder-chip model that mimics the bladder architecture by co-cultures of a well-characterized human bladder epithelial cell line with bladder microvascular endothelial cells in a device geometry that allows the two cells to be exposed to urine and nutritive cell culture media respectively. The flow rates in the apical and vascular channels can be controlled independently, and multiple rounds of micturition are recreated via the application of a linear strain to the PDMS membrane used for co-culture. Using this model, we show that diapedesis of neutrophils to sites of infection on the epithelial side can lead to the formation of neutrophil swarms and neutrophil extracellular traps (NETs), and that IBCs offer substantial protection to bacteria from antibiotic clearance. Our observations suggest that the role of IBCs in reseeding bladder infections upon cessation of antibiotic treatment or

failure to complete a course of antibiotics might be more important than previously assumed and therefore strategies aimed towards eradication of IBCs are very crucial for treatment efficacy.

Results

Reconstitution of bladder uroepithelium and bladder vasculature

We established a bladder-chip infection model by co-culturing HTB9 bladder epithelial cells (epithelial cells) and HMVEC-Bd primary human bladder microvascular endothelial cells (endothelial cells) in a novel bladder-chip approach (Fig. 1A). Immunostaining verified that the epithelial and endothelial cells formed confluent monolayers (cell densities in Table 1) with high expression of junction markers such as epithelial cell adhesion molecule (EpCAM) and platelet endothelial cell adhesion molecule-1 (PECAM-1) and VE-cadherin in the epithelial and endothelial cell layers respectively (Fig 1B, C, additional images in Fig. S1A-H). Expression of these and other junction markers such as E-cadherin and zonula occludins-1 (ZO-1) was consistent across monocultures (Fig. S2A-G) and in co-culture on-chip.

Similarly, a majority of the epithelial cells expressed cytokeratin 7 (CK-7), a general uroepithelial marker and cytokeratin 8 (CK-8), a differentiated uroepithelial marker both in monoculture (Fig. S2I, J) and on-chip (Fig. 1B, S1B, S1F). Some endothelial cells were also CK-7+ (Fig. 1C, S2H). Co-culture of bladder epithelial and bladder endothelial cells in human-bladder chip therefore did not alter the cellular expression patterns of these markers as compared to monocultures. We further characterized the HTB9 cell line in monoculture for markers for urothelial differentiation. HTB9 cells showed high expression of uroplakin-3a (UP3a) which has been shown to be essential for UPEC infection (Fig. S2K) (Martinez et al., 2000; Mulvey et al.,

1998) but only a small proportion of epithelial cells were positive for the basal cell marker cytokeratin1 (CK1), in agreement with the umbrella cell nature of the HTB9 cell line (Fig S2L, M) (Duncan et al., 2004; Smith et al., 2006). Overall, these observations confirmed that the bladder-chip is populated with cells that mimic the physiology of the bladder vasculature and the superficial urothelial cell layer. Further, the chip design enables the flow of media with different compositions through the epithelial and vascular channels. We used this feature to mimic bladder physiology by perfusion of diluted pooled human urine on the epithelial side and endothelial cell medium on the vascular side.

Modelling bladder filling and bladder voiding in the bladder-chip

The human bladder experiences vast changes in volume and surface area on a periodic basis. The first phase of this cycle 'the *filling bladder* state', occurs through a slow and gradual increase in bladder volume due to addition of urine from kidney via the ureters, resulting in a large increase in bladder volume. At the level of the uroepithelium, these changes manifest as a 2-dimensional biaxial stretch with ex vivo studies in rat bladders reporting peak strains of 90 % and 130% measured in the circumferential and longitudinal directions (Gloeckner et al., 2002; Parekh et al., 2010). Subsequently, volume growth slows, and the bladder attains a relatively constant volume, with the bladder epithelium in a corresponding state of maximal stretch '*filled bladder* state'. Voiding of the bladder through urination rapidly reduces bladder volume ('*voiding bladder* state') and removes the strain experienced by the bladder cells. The bladder epithelium, as a viscoelastic material, responds to the removal of strain and relaxes over the subsequent period (Pascalis et al., 2018) where the bladder volume remains low ('*voided bladder* state') (Fig. 1D).

The architecture of the bladder-chip device allows for a linear strain to be applied to the porous membrane via negative pressure in the channels adjacent to the main channel of the device ('the vacuum channels') (Grassart et al., 2019; Huh et al., 2010b) (Fig. 1A). We characterized the strain experienced by epithelial cells due to application of negative pressure (Fig. S3). A plot of applied pressure vs. strain was linear, and we could achieve a dynamic range of linear strain (0 – 19 %) by application of negative pressure (0 – 900 mbar). High levels of applied strain were incompatible with long-term time-lapse microscopy as it generated a significant drift in the axial position of the membrane. We therefore limited the linear strain applied to a maximum of 10%, which is nevertheless a significant proportion of the typical strain experienced by the bladder tissue in vivo. We then modelled the bladder filling and voiding over a 6-hour duty cycle with different states: *filling bladder* (0 - 2hr, 0 to 10% strain), *filled bladder* (2 – 4hr, 10% strain), *voiding bladder* over a period of 2 minutes (4 hr – 4hr + 2min, 10% to 0% strain) and *voided bladder* (4hr + 2min – 6 hr, 0% strain). This 6-hour duty cycle was then repeated for the remaining duration of each experiment. The bladder-chip therefore enables co-culture of two cell-types in nutritionally different microenvironments with a physiologically relevant level of applied strain.

Determination of optimal UPEC infection conditions in the bladder-chip model

UPEC attachment and invasion of bladder epithelial cells has been shown to be sensitive to fluidic shear stress (Andersen et al., 2012; Zalewska-Piątek et al., 2020). Although UPEC infection in the bladder can occur with or without the presence of shear stress, we infected the epithelial layer on the bladder-chip under flow conditions. The small volumes of the microfluidic chip motivated this approach, as rapid bacterial growth in the diluted human urine could lead to

acidification of the medium. We therefore maintained a flow rate of 1.2 ml/hour for a period of 1.5-2 hours during infection of the epithelial layer of the bladder-chips with UPEC. Under flow conditions, an overwhelming majority of bacteria did not attach to the epithelial cells. Time-lapse microscopy showed that bacterial attachment to the epithelial cells increased steadily over this period, but that the typical infectious dose at the end of this period was low (<1 bacterium per epithelial cell, Fig. S4).

Accordingly, we established a 28-hour live-cell imaging experimental protocol as shown in the schematic in Fig. 1E and described in greater detail in the subsequent sections and in methods. Briefly, this consisted of an initial period of homeostasis, followed by UPEC infection, introduction of neutrophils, and two consecutive cycles of antibiotic treatment and recovery to monitor IBC dynamics at the single-cell level. This experimental protocol therefore mimicked key aspects of the host-pathogen interactions in early stages of UTIs as well as the response to antibiotic treatment.

Diapedesis of neutrophils across the epithelial-endothelial barrier in response to UPEC infection in the bladder-chip

The bladder-chip platform enables continuous imaging while maintaining flow in both epithelial and vascular channels and mechanically stretching the membrane as part of the bladder voiding cycle. At the start of each live-cell imaging experiment, bladder epithelial cells in an initial relaxed state were perfused with sterile diluted pooled human urine on the epithelial side and endothelial cell medium on the vascular side respectively (Fig. 2A1, B1, S5A1). The epithelial side was inoculated with a low dose of UPEC in diluted urine and infection was performed under

flow (Fig. 2A2, B2, S5A2) for ca. 1.5 to 2 hours. The first bladder duty cycle also initiated at this timepoint. We maintained the optical focus of the microscope on the epithelial layer over the subsequent course of infection. UPEC attachment was evident during this infection phase by visual inspection (Fig. 2B2, S5A2).

After this period of infection, unattached bacteria in the epithelial channel were removed by perfusion of diluted urine. Our aim was to study the interaction of UPEC with host cells, therefore this perfusion was maintained throughout the experiment. Continuous perfusion reduced the accumulation of bacteria in the urine and enabled imaging of intracellular bacteria without large background noise in the fluorescence channels from planktonic bacteria. We subsequently performed a series of interventions that mimic the course of UTI infections and used time-lapse imaging to monitor the simultaneous changes in host-pathogen interaction dynamics. As a host response, immune cells were introduced into the vascular channel. Among innate immune cells, neutrophils are the first line of defense in UTIs (Haraoka et al., 1999). We isolated neutrophils from human blood through negative depletion and verified that the isolation procedure yielded neutrophils with a high degree of purity (~96% as reported in (Son et al., 2017)) through immunostaining for the anti-CD15 a neutrophil specific marker (Zahler et al., 1997) (Fig. S6). To enable identification and tracking of neutrophils, they were pre-labelled with CellTracker™ Deep Red dye, which stains the cytoplasm of these cells.

Neutrophils were subsequently introduced in the bladder-chip devices through the vascular channel, mimicking the natural route of immune cell migration into the bladder (schematic in Fig. 2A3-A5, snapshots in Fig. 2B3-B5, S5A3-A5). We used a cell concentration of ca. 2 million cells/mL similar to the neutrophil concentration in human blood (Hsieh et al., 2007). During this period, the flow rate through the vascular channel was increased to provide a shear stress $\eta = 1$

dyne/cm^2, which aids neutrophil attachment to endothelial cells (Alon et al., 1995). In uninfected control chips, neutrophil attachment to the endothelial layer was minimal (Fig. S7A, B). Diapedesis of neutrophils to the epithelial layer was rare (Fig. S8A, 2C). In stark contrast, infection of the epithelial layer with UPEC elicited a robust attachment of neutrophils to endothelial cells (Fig. S7C, D) along with a rapid diapedesis across to the epithelial layer (Fig. 2B2-B4, S5A2-A4, S8C). We confirmed that neutrophil diapedesis was also stimulated in the absence of infection, upon exposure to a gradient of pro-inflammatory cytokines that are typically upregulated during UTIs (Agace et al., 1993; Hedges et al., 1992; Nagamatsu et al., 2015; Song et al., 2007) (interleukin-1α, interleukin1-β, interelukin-6 and interleukin-8 each at 100 ng/mL) across the epithelial-endothelial barrier (Fig. S8B). However, neutrophil diapedesis was more robust under infection as compared to the cytokine gradient, with a higher number of neutrophils observed across multiple fields of view on the epithelial side (Fig. S8B-D). These results suggest that infection on-chip generates a strongly pro-inflammatory environment locally and that neutrophil diapedesis is further stimulated by the presence of UPEC(Agace et al., 1995; Oliveira et al., 2016).

Using time-lapse imaging, we were also able to quantify the kinetics of neutrophil migration with a temporal resolution of up to 7.5 minutes. Neutrophil diapedesis to the epithelial sites of infection was detected as early as ca. 15-17 minutes post-introduction into the vascular channel (Fig 2B3, S5A3, supplementary movie SMov1, SMov2). Neutrophils that migrated to the epithelial side aggregated on the epithelial cells (Fig 2B4-2B5, S5A4-A5, supplementary movie SMov1, SMov2) In some cases, these neutrophils were able to control bacterial growth (Fig. 2B4-2B5, dashed yellow boxes) whereas in others, bacterial growth was uncontrolled (Fig. 2B4-

2B5, dashed white boxes). Diapedesis was observed in every field of view examined across n=4 infected chips, whereas diapedesis occurred infrequently in uninfected controls (Fig. 2C). Furthermore, the size of these aggregates was significantly larger in infected bladder-chips vs. uninfected controls, with the aggregates in case of infected-chips exhibiting the characteristic features of neutrophil swarms (Kienle and Lämmermann, 2016; Kreisel et al., 2010; Lämmermann et al., 2013). We quantified the size of the swarms formed by either estimating the maximum number of neutrophils observed in fields of view on the epithelial side (Fig 2D) or by measuring the total volume occupied by neutrophils normalized to the volume of a 3D field of view (Fig 2E). Using either metric, infection generated large swarms that did not occur in uninfected bladder-chips. The dynamic of swarm formation across n=51 and n=40 fields of view in two bladder-chips is shown in Fig. 2F. In these experiments a fast-imaging frequency of 7.5 minutes was used. In infected bladder-chips, swarms reached a maximum size between 60- and 90-minutes post-introduction of neutrophils (Fig. 2G).

Neutrophil extracellular traps (NETs) formation in response to UPEC infection

Neutrophils have complex responses to infections (Oliveira et al., 2016), including the formation of Neutrophil extracellular traps (NETs) that occurs by the release of cytosolic azurophilic granules around a scaffold of decondensed chromatin and potentially serves to trap and kill extracellular bacteria (Brinkmann et al., 2004). NETs have been shown to consist of antimicrobial granules such as myeloperoxidase (Metzler et al., 2011) and neutrophil elastase (Papayannopoulos et al., 2010) and have been observed in urine harvested from UTI patients (Yu et al., 2017). Interestingly, we observed NET formation by neutrophils in the infected bladder-chip. We verified the formation of NETs on the epithelial channel through immunostaining of

infected bladder-chips at 3.5 hours post-infection and 2 hours post-introduction of neutrophils in the vascular channel using antibodies against neutrophil myeloperoxidase (Fig 2H, S9A1-A3) and elastase (Fig 2I, S9B1-B3). In each case, areas on the epithelial layer with strong immunostaining were observed (Fig. 2H3, 2I3). Neutrophils in these areas were typically in large numbers, characteristic of swarms. In addition, by this stage of the experiment, neutrophils that had high levels of myeloperoxidase or elastase typically did not retain strong expression of the cytoplasmic CellTracker dye used for identification of neutrophils in live imaging (cf. Fig. 2H2 and 2H3, 2I2 and 2I3). For each example, a zoomed-in image clearly shows long filament-like structures that extend between cells and are either myeloperoxidase positive (Fig. 2H5) or neutrophil elastase positive (Fig. 2I5), strongly suggestive of NETs (Brinkmann et al., 2004; Metzler et al., 2011; Papayannopoulos et al., 2010). NET formation was also observed in some instances by neutrophils in some locations on the endothelial channel, although large swarms did not form here (Fig. S9B1-B3).

To further characterize these structures, we imaged the epithelial layer of uninfected and infected bladder-chips with or without the addition of neutrophils using scanning electron microscopy (SEM). Representative images of the epithelial layers of uninfected bladder-chip controls (Fig. S10A) contrast with those from infected bladder-chips after neutrophil diapedesis (Fig. 2J1-J4, S10C) and clearly highlight the distinctive features of NET formation. In Fig. 2J1, neutrophils on the surface of the epithelial layer are clearly visible by their distinctive spherical morphology (amber arrowheads). NETs formed between these neutrophils are shown by magenta arrowheads and appear to extend between adjacent neutrophils. A majority of the epithelial cells have a characteristic flattened morphology with cell appendages that can extend between cells (white arrowheads); a highly infected spherical epithelial cell is indicated with a purple arrowhead.

Zooms in Fig. 2J2-2J4 show the structure of NETs in greater detail. Many individual UPEC bacteria (green arrowheads) are captured in these NETs. These structures did not form in infected bladder-chips without the introduction of neutrophils (Fig. S10B), confirming their identity as NETs identified via immunofluorescence. NET formation was a direct response to UPEC and not due to hyperactivation of neutrophils due to experimental handling. To verify this, we collected the neutrophils that passed through an infected bladder-chip without attachment. Even upon infection, an overwhelming majority of the cells perfused into the chip flow out without adhering, because of the geometry of the channels in the device. NET formation in these samples was not observed unless the cells were themselves infected by UPEC shed from the cells in the bladder-chip (Fig. S11).

Heterogenous dynamics of intracellular bacterial communities within urothelial cells

Urinary tract infections that do not resolve upon intervention by the host immune system often require treatment with antibiotics. Antibiotics have complex pharmacokinetic and pharmacodynamic profiles *in vivo*, which we attempted to model through two successive rounds of high dose administration of antibiotics (40x MIC, Fig. S12A), on both the epithelial and vascular side, interrupted by periods with no antibiotic (schematics in Fig. 3A). Continuous time-lapse imaging over this entire period allowed us to capture the responses of bacteria to this simplified model of antibiotic profiles and to study the persistence of UPEC upon antibiotic treatment in the different physiological niches (Fig. 3 and Fig. 4).

A consequence of the first cycle of antibiotic administration under flow was the elimination of extracellular axenic bacterial growth that had occurred in the media in the apical channel, as is observed within the lumen of the bladder *in vivo*. Many that survived the antibiotic treatment

intact did not regrow after the antibiotic was removed (Fig. S12 B). Regrowth commenced in only a small fraction of bacteria (Fig. S12C) after a variable lag phase (Fig. S12D) and rapid regrowth was highly correlated with intracellular location of bacteria within epithelial cells. These subsequently proceeded to form intracellular bacterial communities (IBCs), with a variable lag period. An example of an early stage of the IBC formation is shown in the timeseries in Fig. 3B1-B5, supplementary movie SMov3. This IBC was initially seeded with few bacteria that are present in Fig. 3B1 and clearly visible in Fig. 3B2. At the end of the timeseries, the entire host cell was packed with bacteria (Fig. 3B5). The exponential increase in bacterial numbers frequently led to the saturation of the 8-bit images in the bacterial channel. We therefore examined similar structures in separate bladder-chips via immunofluorescence (Fig. 3C, S13) staining. Zooms of two of the four IBCs highlighted in Fig. 3C show numerous tightly packed bacteria within epithelial cells that are both CK7+ (Fig. 3C) and CK8+ (Fig. S13). These bacterial morphologies are highly similar to early-stage IBCs observed in the bladder(Anderson et al., 2003; Justice et al., 2004). Higher resolution images of the biofilm-like structures within IBCs obtained via correlative light (Fig. 3D) and transmission electron microscopy (Fig. 3E) showed that bacteria in IBCs can be either coccoid or rod shaped, which is also evident in scanning electron micrographs of bacteria within IBCs (Fig. 3F). IBCs within bladder-chip model therefore show many of the distinctive morphological features reported from images of infected bladders in the mouse model (Anderson et al., 2003; Hunstad and Justice, 2010).

Numerous reports from the mouse model of infection have shown IBCs to be dynamic structures; growth in IBCs eventually culminates in bacterial shedding or the complete exfoliation of the IBC. The underlying dynamics of these phenotypes is hard to capture in the mouse model, but

the bladder-chip model allowed us to track the dynamics of bacterial growth within individual IBCs over extended periods of time, providing information on bacterial dynamics within so-called early, middle and late-stage IBCs. An example of the heterogeneity in growth rates is evident from the timeseries for three IBCs in Fig. 3G1-G3, supplementary movie SMov4. IBCs#1 and 2 subsequently began to shed individual bacteria (Fig. 3G4), a phenotype not observed in IBC#3. At a later timepoint (Fig. 3G5) the fates of all three IBCs were dramatically different – the cell containing IBC#1 had completely exfoliated and was removed from the field of the view by flow in the epithelial channel, IBC#2 continued to shed bacteria, whereas growth remained slow in IBC#3. We monitored the eventual fate of n=100 IBCs during the first and the second growth cycles which confirmed that shedding and exfoliation were not mutually exclusive. While some IBCs only shed bacteria (n=28) and others exfoliated without shedding (n=27), a substantial fraction of IBCs showed shedding prior to exfoliation (n=31) and some IBCs displayed neither phenotype (n=14). Furthermore, in addition to the coccoid and rod-shaped morphologies highlighted in Fig. 3C-F, time-lapse imaging also enabled us to capture events that occurred relatively rarely such as the intracellular growth of filamentous forms of UPEC (Fig. 3H1-H5, S14, supplementary movie SMov5, SMov6). In this time series, a filamentous bacteria can be seen and appears to encircle the inner boundary of the cell (Fig. 3H1-3H4) before filling the volume entirely (Fig. 3H5). Overall, time-lapse imaging confirms that a significant fraction of bacteria within IBCs can survive the first round of antibiotic treatment and are the source for reseeding of both the extracellular bacterial populations as well as the subsequent growth of IBCs in newly infected cells.

Dynamic persistence of intracellular bacterial communities within urothelial cells

A subsequent round of antibiotic treatment provided an opportunity to study the dynamic persistence of bacteria within IBCs in response to an antibiotic profile that was a closer mimic of the varying antibiotic concentrations in vivo. Furthermore, at this stage of the experiment, we were also able to study the responses of bacteria in middle and mature late-stage IBCs to antibiotic treatment which was not possible during the first round of antibiotic administration early in the course of infection. In the examples highlighted in Fig. 4A1-A5 and supplementary movie SMov7, bacterial growth after the first round of antibiotic treatment resulted in the formation of many large IBCs with tightly packed bacteria (Fig. 4A1-A2). Many of the bacteria within each of the four IBCs were eliminated by the antibiotic, but a substantial proportion of bacteria in each IBC nevertheless survived the antibiotic treatment (Fig. 4A3). Each of these IBCs subsequently regrows when the antibiotic is removed (Fig. 4A4-A5), and two additional IBCs are seeded during this time (white arrowheads in Fig. 4A5). Overall, the second round of antibiotic administration led to a sharp decline in instances of subsequent bacterial regrowth (Fig. S12C). In all instances, regrowth either occurred directly within IBCs, or was caused by the shedding of bacteria from IBCs to repopulate the extracellular niche and seed new IBCs, highlighting the dynamic stability of this niche and its importance in establishing persistent infection. We therefore performed a careful analysis to quantify bacterial growth rate within IBCs. Growth within IBCs across different time periods was exponential (Fig. 4B). We were able to track a subset of IBCs across two growth cycles (Fig. 4C). In a majority of instances these revealed exponential growth in the absence of antibiotic, delayed response to antibiotic, and a lag phase after the antibiotic was removed. In general, bacterial growth in IBCs in the second growth cycle was slower than in the first (Fig. 4D). However, this population level statistic may be influenced by the fact that many of the IBCs monitored in the second growth cycle had been

exposed to two rounds of antibiotic treatment. For this sub-population, in n=16 out of n=18 IBCs, growth was slower after the 2nd round of antibiotic administration (Fig. 4E).

Next, we examined the dynamics of bacterial growth within IBCs during the period of antibiotic treatment in greater detail. In the IBC shown in the timeseries in (Fig. 4F1-4F5, S15A1-A5, supplementary movie SMov8, SMov9), growth before antibiotic administration (Fig. 4F1, 4F2) continued for a considerable period after the antibiotic was administered (Fig. 4F3, Fig. 4F4, S15A1-S14A3). Eventually, a reduction in bacterial volume towards the end of the antibiotic administration period was observed (Fig. 4F5, S15A4-S15A5). In contrast, the relatively smaller IBC in the timeseries in Fig. 4G1-4G5, S15B2-S15B5, supplementary movie SMov10, SMov11 continued to grow throughout the period of antibiotic administration. These different dynamics are also captured in the plot of bacterial volume for multiple IBCs before, during, and after the antibiotic treatment. In all cases, bacterial volume continues to increase during a significant period of antibiotic administration (Fig. 4H), and in 2 out of 18 cases, there was no decrease in bacterial volume throughout this period. In contrast, extracellular bacteria likely adherent on the epithelial cells but not internalized within them were rapidly eliminated by combination of antibiotic treatment and flow (Fig. 4I), in all cases the bacterial volume reduced immediately upon antibiotic administration. This differential killing resulted in a significantly higher proportion of extracellular population of bacteria being killed (Fig. 4J). Elimination of bacteria within IBCs was highly heterogenous. Another consequence of this differential killing was that after the 2nd round of antibiotic treatment, regrowth was observed in only a very small fraction of non-IBC UPEC (Fig. S12C). Protection of bacteria within IBCs therefore has a direct outcome of enabling the reseeding of infection at other locations within the epithelial monolayer.

Lastly, we sought to determine if the bladder duty cycle altered the dynamics of UPEC infection. A comparison between infected bladder-chips with and without the duty cycle (Fig. 4K, L, S16) revealed a significant increase in the bacterial burden when the duty cycle was implemented (Fig. 4M). These results suggest that the bladder filling and voiding cycle influence the uptake and proliferation of UPEC, possibly through physiological changes in the epithelial cells in response to applied strains (Apodaca, 2004; Carattino et al., 2013; Truschel et al., 2002; Wang et al., 2005). In turn, they suggest a deeper connection between the physiology of mechanically active organs such as the bladder and infection, which can be probed further in the bladder-chip model.

Discussion

In our human bladder-chip model we focus on recapitulating the key aspects of bladder physiology relevant to the study of the earliest stages of UPEC infection and IBC formation. Therefore, superficial bladder epithelial cells, the first cell-type usually infected by UPEC, are cultured both under flow in diluted pooled urine and in co-culture with bladder microvascular endothelial cells. The ability to apply a cyclic mechanical stretch to the PDMS membrane, originally designed to mimic the breathing motion in the lung (Huh et al., 2010b) or the peristaltic motion in the gut (Kim and Ingber, 2013), has been adapted here to mimic the slow expansion and rapid contraction of bladder volume. We demonstrate the ability to perform multiple duty cycles while simultaneously imaging the infected device via long-term time-lapse imaging, a technical advance that is difficult to achieve with bladder explants (Justice et al., 2004) or other *in vitro* studies of UPEC infection of bladder epithelial cells (Andersen et al., 2012; Horsley et al., 2018; Iosifidis and Duggin, 2020; Smith et al., 2006). Using this approach,

we found that the total bacterial burden inside infected bladder-chips was significantly higher at a late stage of infection if a duty cycle was applied, unlike the non-significant influence of cyclic stretching on Shigella infection of intestinal-chips under flow conditions (Grassart et al., 2019). The exact mechanisms underlying this phenomenon remain to be explored, but there is an increasing understanding of the role of mechanical forces in regulating innate immune function (Solis et al., 2019). Our results showcase the ability of the bladder-chip model to capture these interactions between mechanical function, physiology and infection, unlike other infection models reported thus far.

A primary focus of *in vitro* models developed so far has been to probe specific aspects of UPEC infection, such as the role of the stratified bladder architecture (Horsley et al., 2018) or the effects of micturition on IBC formation (Andersen et al., 2012; Iosifidis and Duggin, 2020). However, the migration of immune cells into the bladder in immune cells is difficult to reproduce in these models, and in many of these systems, live-cell imaging remains technically challenging (Horsley et al., 2018; Smith et al., 2006). Furthermore, the models do now allow mechanical manipulations of the cellular co-culture. In that sense, the bladder-chip model complements these existing approaches by providing these additional functionalities. Further development, potentially through the combination of organoid and organ-on-chip approaches, could lead to the development of a fully stratified urothelium on-chip, although the utility for studying IBC dynamics is relatively limited.

Neutrophils are the first responders to UPEC infection (Abraham and Miao, 2015; Haraoka et al., 1999), and neutrophil migration involves a series of steps that commences with attachment to the endothelium under flow, migration on the endothelial surface, diapedesis across the epithelial-

endothelial cell barrier and movement towards the site of infection (Ley et al., 2007; Nourshargh et al., 2010). Perfusion of the vascular channel with CD15+ neutrophils isolated from human blood shows that the bladder-chip model recapitulates all of these phenotypes, with rapid diapedesis of neutrophils to sites of infection. There, neutrophils aggregate to form swarms (Kienle and Lämmermann, 2016; Lämmermann et al., 2013) and subsequently, the formation of NETs (Branzk et al., 2014; Brinkmann et al., 2004; Metzler et al., 2011; Papayannopoulos et al., 2010) around extracellular bacteria is observed. Characterization of these structures via SEM shows that they can extend across many tens of microns and stain positive for myeloperoxidase (Metzler et al., 2011) and neutrophil elastase (Papayannopoulos et al., 2010), indicative of potent anti-microbial activity. However, neutrophil control of infection on-chip is partial; this is possibly due to the unrestricted growth of large numbers of extracellular bacteria and in some instances, exacerbated by the loss of some neutrophils due to flow in the channel. Another contributing factor could potentially be the architecture of the PDMS membrane, which permits neutrophil diapedesis only at fixed spatial locations on-chip. Neutrophil migration may also be impacted by the relative stiffness of the PDMS membrane. Nevertheless, the demonstration of NET formation is consistent with the occurrence of these structures both in the mouse model (Ermert et al., 2009) as well as in the urine of infected patients (Yu et al., 2017) and suggests that the model is able to recapitulate important aspects of disease. It is also an important advance for the use of organ-on-chip approaches to recapitulate NET formation in infectious disease.

IBC formation begins immediately after infection and is already underway upon neutrophil administration. However, clear demonstration of IBCs with a high degree of confidence was only possible after an initial treatment with a high dose of antibiotic that eliminated extracellular

planktonic bacteria and improved the optical imaging of bacteria attached to or within the epithelial cells. It enabled us to capture the full cycle of IBC growth from 1-2 bacteria to a large biofilm and subsequent release via shedding and filamentation. Importantly, the compact nature of the device allowed us to image multiple IBCs concurrently on the same chip with a high temporal resolution, which is difficult to achieve in bladder explants (Justice et al., 2004). Our observations reiterate the highly dynamic nature of these structures; growth was asynchronous and heterogenous and outcomes included bacterial shedding, exfoliation and filamentation (Hunstad and Justice, 2010; Justice et al., 2004; Scott et al., 2015). Notably, shedding and exfoliation were not mutually exclusive for the time-period of our observations – we report examples of IBCs that shed bacteria and contract in volume before exfoliation.

While IBCs are clearly acknowledged as critical players in early infection, the contribution towards promoting persistence is not completely understood. For example, Blango *et al*. (Blango and Mulvey, 2010) showed that incubation of bladder explants containing IBCs with a high dose of antibiotics for a period of 18 hours resulted in a substantial sterilization of these structures and concluded that other populations, notably quiescent reservoirs (Mysorekar and Hultgren, 2006) might play a greater role in the establishment of persistent populations. However, the pharmacokinetic profiles of most antibiotics in the host are not time-invariant. In case of ampicillin, a standard regimen of ampicillin treatment is typically a bolus of 250-500 mg of antibiotic administered every 6 hours. Within the serum, ampicillin concentration peaks at a C_{max} ~ 3-40 μg/ml, which is between 1.5 to 20-fold the MIC as measured in human serum (Bryskier, 2020; Putrinš et al., 2015). These values are in good agreement with the concentrations we use, that are 40-fold higher than the MIC measured in the endothelial medium perfused in the

vascular channel. Ampicillin concentrations in the blood rapidly decay with a half-life of between 60 and 90 minutes with a characteristic pharmacokinetic/pharmacodynamic profile. This period is modelled well by our experimental protocol where phases with high concentration of ampicillin are interspersed with periods with no antibiotic. We are therefore able to model the delivery of two consecutive doses of antibiotic and find that IBCs offer substantial protection against sterilization by a short duration of a high-dose antibiotic treatment and in many instances, bacterial regrowth after two successive rounds of antibiotic administration. Notably, in smaller 'early IBCs', bacterial growth continues throughout the period of ampicillin administration, suggesting that the intact nature of the cell membrane likely diminishes the effect of the drug. Our results suggest that, IBCs may continue to play a role in reseeding sites of infection for a considerable period after the commencement of antibiotic treatment. This has particularly important implications with regard to the compliance of antibiotic use as proliferating IBCs could rapidly re-seed sites of infection throughout the bladder if antibiotic doses are missed. These unique capabilities of the bladder-chip to realistically model antibiotic treatment regimens for IBCs can in the future be leveraged to screen compounds (Spaulding et al., 2017) and identify optimal antibiotic regimens, treatments that can eliminate persistent bacterial populations in IBCs or alter the host-pathogen interaction dynamic in UTIs.

In summary, the bladder-chip model incorporates aspects of bladder physiology highly relevant to early UPEC infection in a platform amenable to long-term live-cell imaging as well as for the administration of antibiotics and therapeutics in a physiologically relevant manner. Our results establish the suitability of this model for immunological and drug-delivery studies and show that

IBCs are highly dynamic structures that offer substantial protection from antibiotic clearance for an extended period of time.

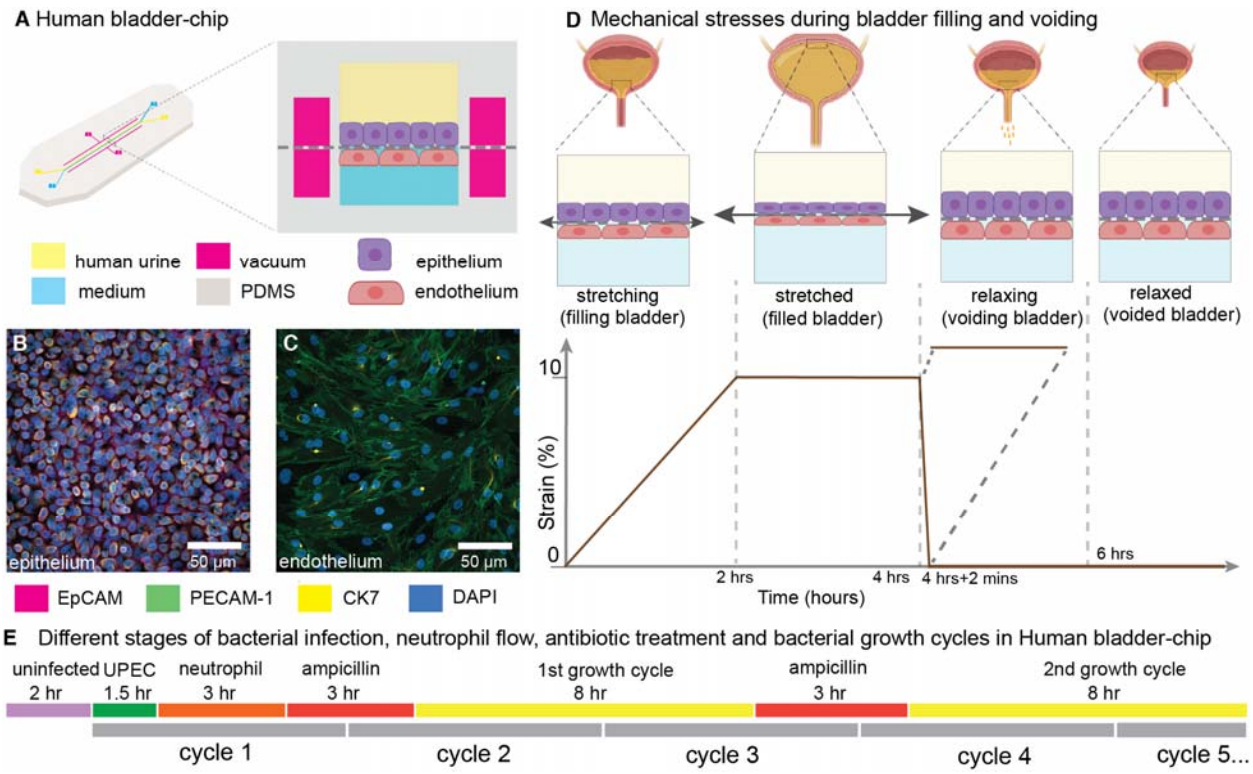

Figure 1: Human Bladder-chip model of UTI recapitulates the physiology of bladder filling and voiding.
(A) Schematic of the human bladder-chip with co-culture of the HTB9 human bladder epithelial cell line (epithelium, top) and primary human bladder microvascular endothelial cells (endothelial, bottom) on either side of the stretchable and porous membrane. Pooled human urine diluted in PBS and endothelial cell medium were perfused in the apical and vascular channels respectively to mimic bladder physiology. A negative pressure in the 'vacuum' channels (magenta) on either side of the main channel was applied to stretch the porous membrane to mimic stretching of the bladder. (**B**, **C**) Immunofluorescence staining of confluent epithelial and endothelial cell monolayers (anti-EpCAM (magenta) and anti-CK-7 (yellow) for the epithelial cells and anti-PECAM-1 (green) for the endothelial cells) in an uninfected control chip. Some endothelial cells also stained positive for CK7. Cell nuclei were labeled with DAPI (azure). (**D**) Schematic of the reconstitution of the bladder filling and voiding cycle via stretching of the membrane with a duty cycle of 6 hours. The cycle consisted of a linear increase in strain through

stretching of the membrane (*filling bladder*, 0 - 2 hours), maintenance of the membrane under stretch (*filled bladder*, 2 - 4 hours), a quick relaxation of applied strain over 2 minutes (*voiding bladder*, 4hr+2 min) and maintenance without applied strain (*voided bladder*, 4hr+2min - 6hr). (**E**) An overview of the timeline of the experimental protocol including infection, addition of neutrophils via the vascular channel, and two cycles of antibiotic treatment interspersed by two bacterial growth cycles. The consecutive bladder duty cycles are indicated.

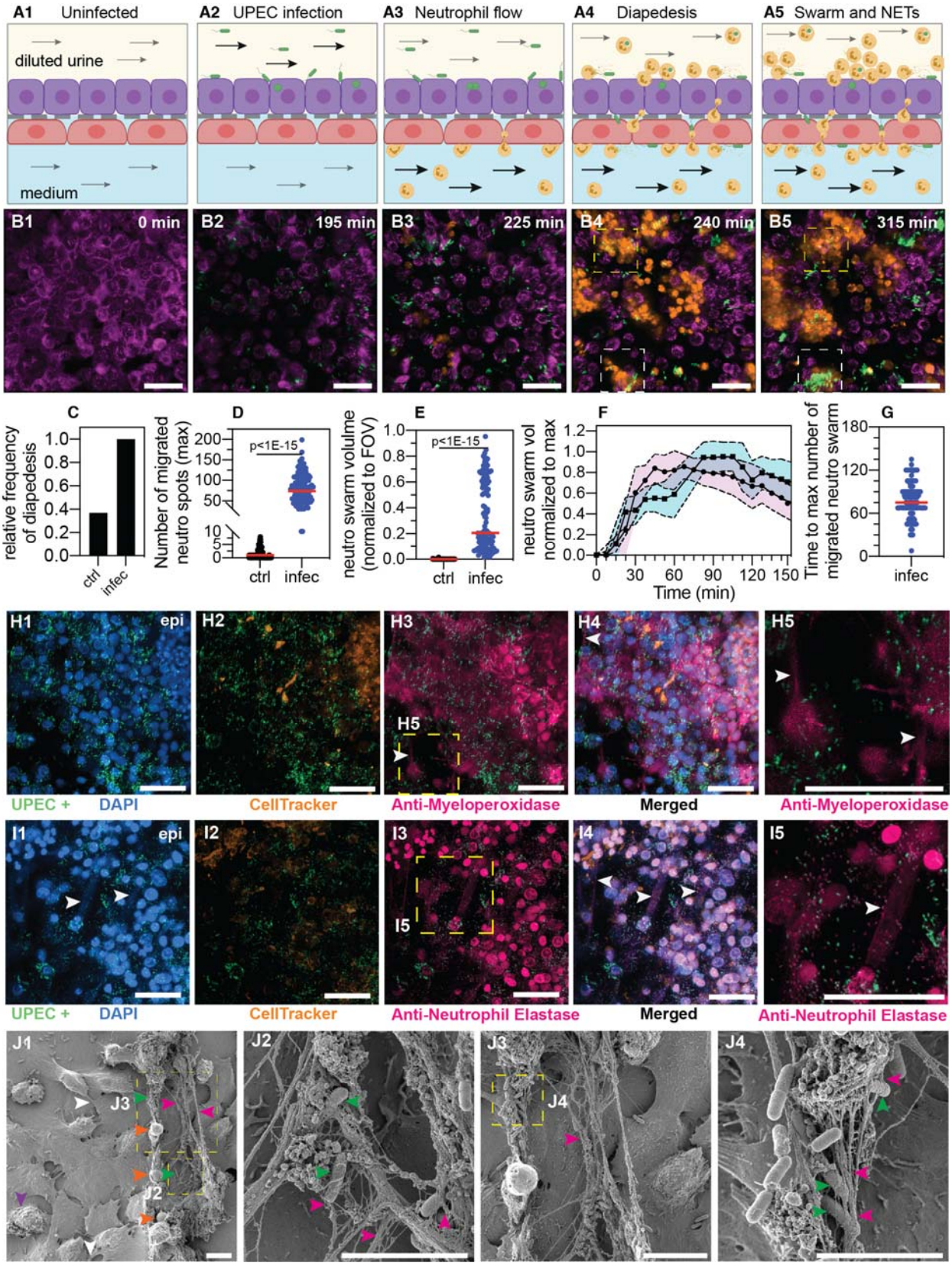

Figure 2: Neutrophil diapedesis and NET formation on-chip

(**A1-A5**) Schematic of the UPEC infection, introduction of neutrophils and diapedesis of neutrophils across the epithelial-endothelial barrier to sites of infection. Flow in the epithelial and endothelial channels is indicated by arrows; the flow rate was increased upon introduction of neutrophils in the vascular channel to enable optimum attachment. (**B1-B5**) Snapshots from time-lapse imaging highlighting each stage in the infection cycle shown in (**A1-A5**). Bladder epithelial cells (magenta) and neutrophils (amber) were identified with membrane (Cell Mask Orange) and cytoplasmic (Cell Tracker Deep Red) dyes, respectively. UPEC identified via constitutive expression of YFP are shown in green. Neutrophil swarms could either control bacterial growth (yellow dashed square, compare B4 vs B5) or did not manage to restrict bacterial growth (white dashed square, compare B4 vs B5). (**C**) Bar charts for relative frequency of neutrophil diapedesis (black) in n=3 uninfected control bladder-chips and n=4 infected bladder-chips. Data obtained from n=95 and n=116 across 206 x 206 μm^2 fields of view. (**D**) Quantification of the number of neutrophils detected on the epithelial layer, in control and infected bladder-chips. The red bar represents the median value. $p<1E-15$. In many instances in the uninfected control bladder-chips, no neutrophil diapedesis is detected. (**E**) A plot of the maximum neutrophil swarm volume on the epithelial layer normalized to the total volume for n=67 and n=118 fields of view on n=3 uninfected control and n=3 infected bladder-chips. (**F**) A plot of neutrophil swarm volume on the epithelial layer over time for n=51 and n=40 fields of view for n=2 technical replicates indicated by squares and circles. For each time profile, the volume is normalized to the maximum volume attained over the timeseries and t=0 refers to the timepoint at which neutrophils are introduced into the vascular channel (**G**) Plot of the time to the reach the maximum swarm volume in n=154 fields of view across n=4 infected bladder-chips. (**H1-H54, I1-I5**) NET formation by neutrophils on the epithelial layer. The neutrophils are

identified by a cytoplasmic dye (CellTracker Deep Red, false coloured in amber) (**H2, I2)** and immunostaining with an anti-myeloperoxidase antibody (**H3,** zooms in **H5**) or an anti-neutrophil elastase antibody (**I3,** zooms in **I5**). Merged images in each case are shown in **H4** and **I4**. UPEC identified via YFP expression is shown in spring green. Nuclear labelling with DAPI is shown in Azure. (**H5**) NETs, identified via anti-myeloperoxidase staining or anti-elastase staining are indicated with white arrows in (**H5**) and (**I5**) respectively. (**J1**) Scanning electron micrographs of the epithelial layer of an infected bladder chip 2 hours after the introduction of neutrophils in the endothelial channel. Neutrophils, (amber arrowheads,) are visible above a layer of epithelial cells. A heavily infected epithelial cell (purple arrowhead), NETs produced by the neutrophils (magenta arrowheads), individual UPEC bacteria within the NETs (green arrowheads) are visible. Appendages between epithelial cells are indicated by white arrowheads. (**J2**, **J3**) Zooms of the regions in **J1** identified by white squares that highlight the structure of two distinct NETs. (**J4**) Zoom of the region in **J3** identified by a yellow square. Scale bar = 50 μm in **B1-B5**, **H1-H5, I1-I5** and 20 μm in **J1-J5**.

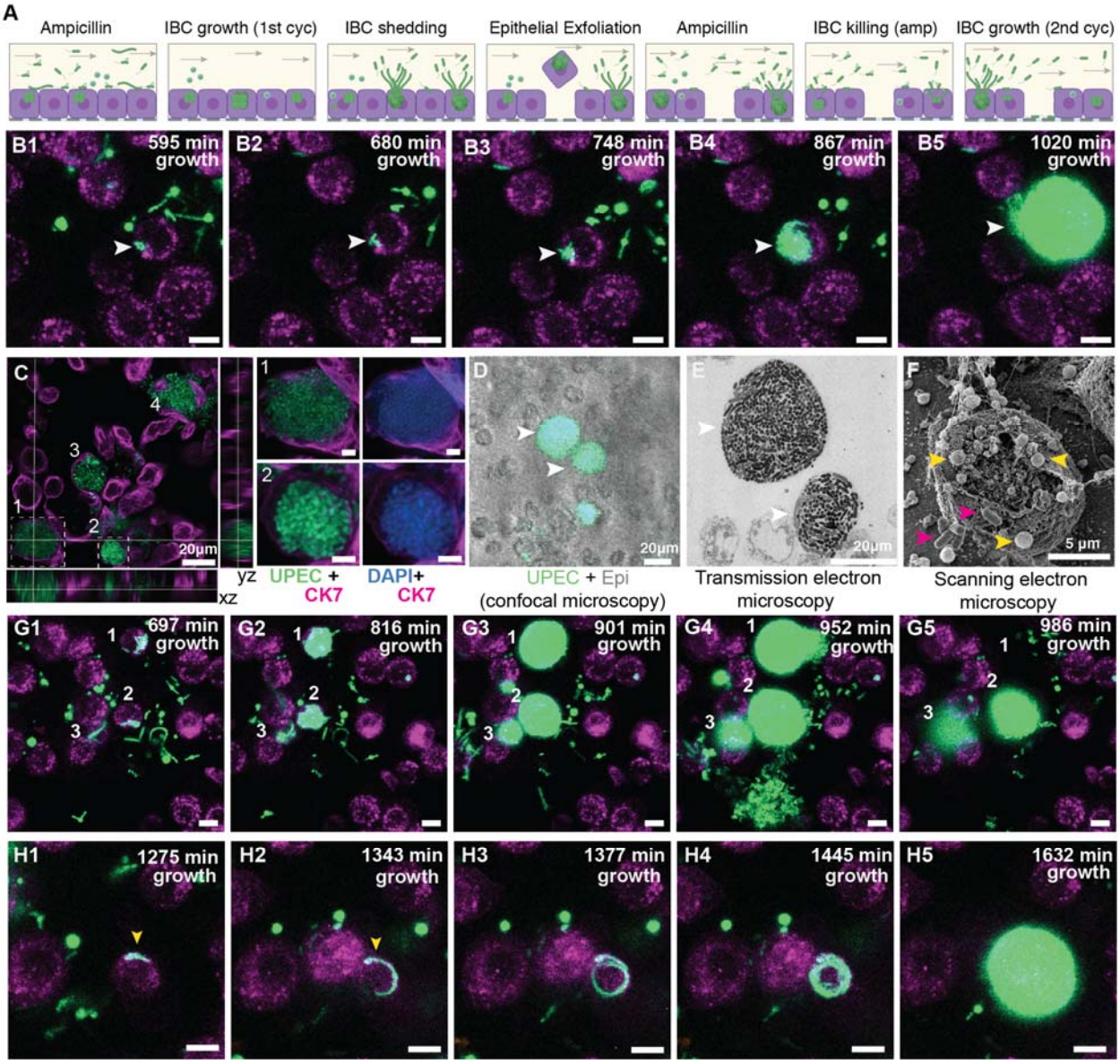

Figure 3: Bladder-chip reveals dynamics of IBC growth, shedding and exfoliation. (**A**) Schematics of the host-pathogen interactions within IBCs between successive rounds of antibiotic treatment with outcomes including shedding of bacteria and cell exfoliation shown. (**B1**-**B5**) Timeseries for the growth of an IBC from few bacteria (white arrowhead) after the first round of ampicillin treatment. Bacteria grow to completely fill the cell volume (**B5**). (**C**) Immunofluorescence characterization of two IBCs; the intracellular nature of growth is confirmed with staining with an anti-CK7 antibody. Correlative light (**D**) and transmission

electron micrographs (**E**) show two IBCs filled with both rod-shaped and coccoid-shaped bacteria. (**F**) Coccoid shaped bacteria (yellow arrowheads) and rod-shaped bacteria (magenta arrowheads) are also visible in a scanning electron micrograph of an infected epithelial cell. IBCs on infected bladder chips shown in C-F were fixed 13 hours after UPEC infection and 6 hours into the 1st growth cycle. (**G1-G5**) Three examples of IBC growth, labelled 1 – 3 with differing outcomes. Unrestricted bacterial growth is observed within all IBCs. In IBC#1 at timepoint (**G4**) the IBC begins to shed bacteria into the surrounding medium. The cell exfoliates in the time interval between (**G4** and **G5**). In IBC#2, bacterial shedding is visible at (**G4**) and shedding continues until end of the timeseries with a reduction in bacterial volume. In contrast, growth within IBC#3 is slower and neither shedding nor exfoliation occurs within the timeseries. (**H1-H5**) Timeseries highlighting an example of filamentous UPEC growth within an IBC. Scale bars, 10 μm in **B1-B5**, **G1-G5** and **H1-H5**.

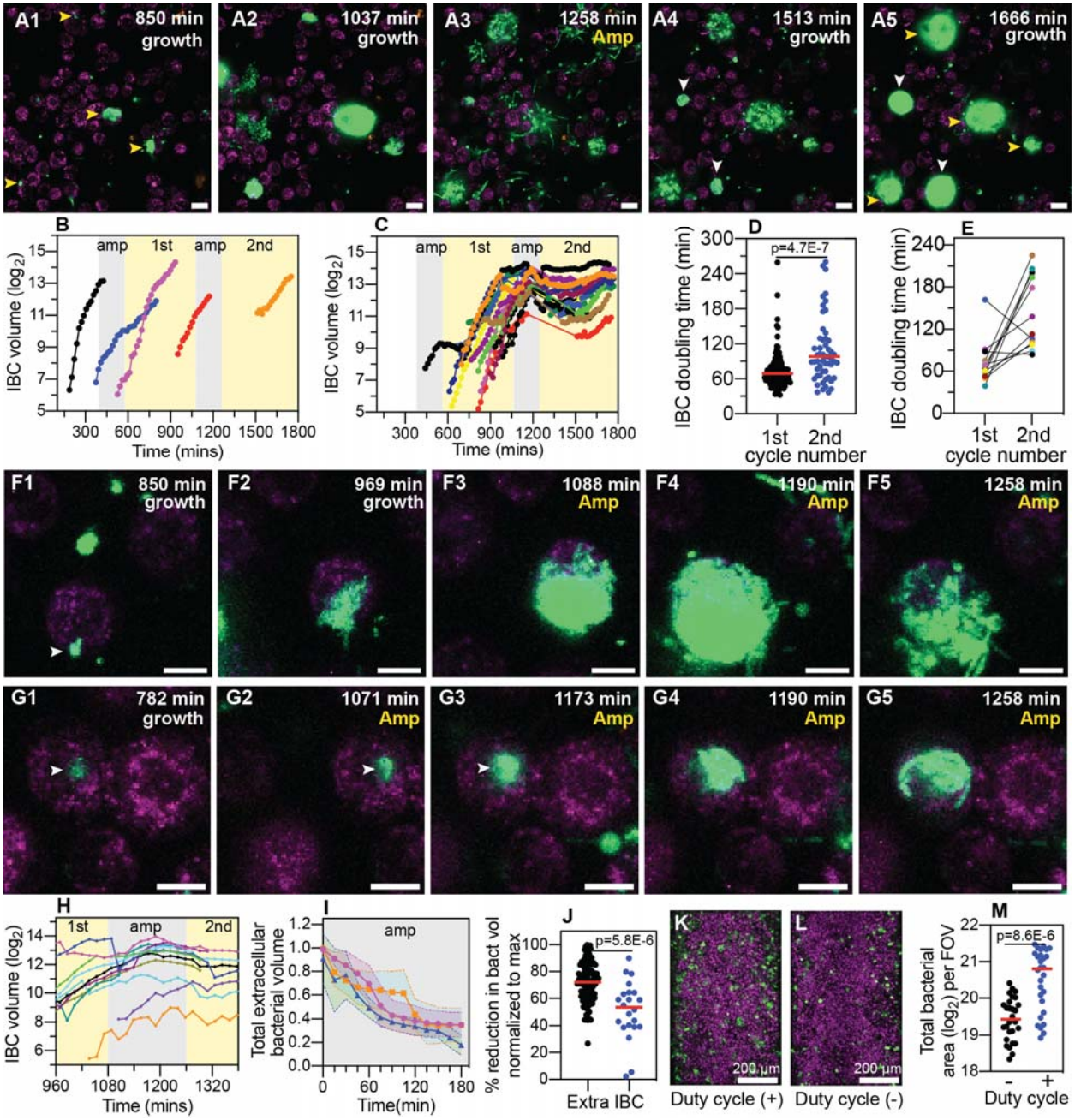

Figure 4: IBCs offer a semi-protective niche that delays clearance of bacteria by antibiotics. (**A1-A5**) Bacteria persist and grow in IBCs despite antibiotic treatment. Snapshots show the growth of four IBCs with variable growth rates (**A1-A2**). Ampicillin treatment eliminates some but not all of the bacteria within each IBC (**A3**). Growth resumes at all sites in (**A4**, **A5**), formation of new IBCs in the 2nd growth cycle is indicated by white arrowheads. (**B)** Plots of

logarithm of bacterial volume within five separate IBCs show a linear increase in volume over time, suggesting bacterial growth is exponential. IBCs are seeded dynamically; growth can occur either in the first or second growth cycle, or prior to the administration of antibiotic, or in few cases continues in the presence of the antibiotic. (**C)** Plots of the logarithm of bacterial volume vs. time for n=18 IBCs tracked across two growth phases with an intermediate period of ampicillin treatment. In the growth phases, growth is exponential and bacterial volume continues to increase for up to ca. 120 minutes after administration of antibiotic before declining due to loss of bacteria. In each case, growth resumes after the antibiotic is removed. (**D**) Scatter plots of the doubling time of bacterial volume in IBCs as measured in the first growth cycle (n=102) and the second growth cycle (n=59). Growth in the second cycle is significantly slower (p=4.7E-7), red line represents the median value. P-values calculated using a Mann-Whitney test. (**E**) Doubling time of bacterial volume in IBCs in the first and second growth cycle for some of the IBCs in (**D**) that survived the antibiotic treatment. In n=16 out of 18 instances, growth is slower in the second growth cycle. (**F1-F5**) High resolution time-series that highlights bacterial growth within an IBC prior to (**F1**, **F2**) and after (**F3-F5**) administration of ampicillin. Some bacteria within this IBC are subsequently eliminated (**F5**). (**G1-G5**) High resolution time-series that highlights bacterial growth within an IBC prior to (**G1**, **G2**) and after (**G3-G5**) administration of ampicillin. The bacterial volume within this IBC is not diminished by antibiotic treatment (**G5**). (**H)** Plots of logarithm of bacterial volume within n=11 IBCs before, during, and after the second round of antibiotic treatment. (**I**) Plot of the volume of extracellular bacteria upon antibiotic administration from n=103 across 206 x 206 μm^2 field of view from n=3 bladder-chips. (**J**) Scatter plot of the extracellular bacterial volume (n=105) and bacterial volume within IBCs (n=22) after antibiotic treatment as a fraction of the maximum bacterial volume prior to

antibiotic treatment. Red line represents the median value, p=1E-9 as calculated by Mann-Whitney test. (**K**, **L**) Representative images from the epithelial face of the infected bladder-chips with or without duty cycle. (**M**) Scatter plots of the logarithm of the total bacterial area across n=14 from infected bladder-chips with (n=2) and without (n=2) duty cycle. p= 8.6E-6 as calculated by the Mann-Whitney test. Infected bladder chips shown in **K**, **L** were fixed 13 hours after UPEC infection and 6 hours into the 1st growth cycle. Scale bars, 10 μm in panels **A1**-**A5**, **F1**-**F5**, and **G1**-**G5**.

Cell type	**Cell density/$10^4 \mu m^2$**
Epithelial	31.7 ± 5.1
Endothelial	4.0 ± 0.6

Table 1.

Characterization of epithelial and endothelial cell densities from n=2 bladder-chips

Acknowledgements

V.V.T gratefully acknowledges support by a Human Frontier Science Program (HFSP) Long-Term Fellowship (LT000231/2016-L) and a European Molecular Biology Organization (EMBO) Long-Term Fellowship (921-2015). This research was supported by a grant awarded to J.D.M by the Swiss National Science Foundation (SNSF) (Project Funding, 310030B_176397). The authors thank the entire team of EPFL Bioimaging & Optics Core Facility for their assistance in confocal live cell imaging and post analysis in Bitplane Imaris. The authors also acknowledge the tremendous help provided by Dr. Graham Knott and Marie Croisier (at the EPFL Biological Electron Microscopy Facility) for help in optimizing the protocol for TEM of infected bladder-chip. The authors would like to thank and credit BioRender.com for the illustrations and schematics used in this manuscript.

654 **Materials and Methods**

Reagent or resource	Designation	Source or reference	Identifiers	Additional information
strain, strain background ()	Uropathogenic Escherichia coli (UPEC) strain CFT073	PMID: 2182540	NCBI: txid199310	originally isolated from a pyelonephritis patient and provided by Prof. H.L.T. Mobley, University of Michigan, USA
strain, strain background ()	CFT073-pZA32-YFP	this paper		constructed by Dr. Neeraj Dhar (this study)
biological sample (*Mus musculus*)	HTB-9™ bladder epithelial cells	ATCC	Cat#:5637	
biological sample (*Mus musculus*)	HMVEC-Bd – Human Bladder Microvascular Endothelial Cells	Lonza	Cat#:7016	
other	RPMI-1640 medium	ATCC	Cat#:30-2001	
other	Gibco™ RPMI 1640 Medium, no phenol red	Thermofisher	Cat#:11835063	
other	Gibco™ Fetal Bovine Serum, Premium Plus	Thermofisher	Cat#: A4766801	
other	EGM™-2 MV Microvascular Endothelial Cell Growth Medium-2 BulletKit™	Lonza	Cat#:CC-3202	
other	EBM-PRF Endothelial Medium Phenol-red free, 500 ML	Lonza	Cat#:CC-3129	
other	EGM™-2 Endothelial SingleQuots™ Kit	Lonza	Cat#:CC-4176	
other	Gibco™ Antibiotic-Antimycotic (100X)	Thermofisher	Cat#:15240062	
other	Gibco™ Trypsin-EDTA (0.05%), phenol red	Thermofisher	Cat#:25300054	
drug	Chloramphenicol			34 mg/ml in ethanol (stored at -20 ^{o}C)
drug	Ampicillin	Sigma-Aldrich	Cat#: A9518-5G	50 mg/ml in ddH_2O (stored at -80 ^{o}C)
other	pooled human female urine	Golden West Diagnostics	Cat#: OH2010-pH	
other	Phosphate Buffered Saline	Thermofisher		
other	Gibco™ HEPES	Thermofisher	Cat#: F2006	
other	Invitrogen™ DAPI	Thermofisher	Cat#: D1306	5 mg/ml in DMSO
other	LB Broth (Luria low salt)	Sigma-Aldrich	Cat#: L3397-1KG	
other	Organ-chips (Standard Research Kit - 24 per	Emulate	RE1000001024	Emulate, Inc. 27 Drydock Ave, 5th

	Pack)			Floor Boston, MA 02210
other	CellMask™ Orange Plasma membrane Stain	Thermofisher	Cat#: C10045	
other	HCS CellMask™ Deep Red Stain	Thermofisher	Cat#: H32721	
other	CellTracker™ Deep Red Dye	Thermofisher	Cat#: C34565	
other	Elveflow® OB1 Pressure Controller OB1 Base MkIII+	Elveflow	Cat#: OB1MKIII+-MIX-	connected to 6bar compressed air channel
other	Elveflow® OB1 Pressure Controller OB1 MkIII Channel-900/1000	Elveflow	Cat#: OB1-Dual-	connected to Elveflow® OB1 Pressure Controller OB1 Base MkIII+
other	Diaphragm moist gas vacuum pump	KNF Neuberger	Cat#:LABOPORT ® UN 820.3 FT.40P	connected to Elveflow® OB1 Pressure Controller OB1 MkIII Channel-900/1000
antibody	Anti-EpCAM	abcam	Cat#: ab71916	used at 1:100 dilution in 1% BSA, conjugated with Donkey anti-Rabbit secondary antibody, Alexa Fluor 647 (2µg/ml) and Alexa Fluor 568 (2µg/ml) in 1%BSA
antibody	Anti-PECAM1 or Anti-CD31	abcam	Cat#: ab24590	used at 1:100 dilution in 1% BSA, conjugated with Donkey anti-Mouse secondary antibody, Alexa Fluor 647 (2µg/ml) and Goat anti-Mouse Alexa Fluor 488 (2µg/ml) in 1%BSA
antibody	Anti-CK7	abcam	Cat#: ab209599	used at 1:100 dilution in 1% BSA
antibody	Anti-CK8	abcam	Cat#: ab192468	used at 1:100 dilution in 1% BSA
other	Alexa Fluor™ 555 Phalloidin	Thermofisher	Cat#: A34055	used at 1µM concentration in PBS
antibody	Anti-VE-Cadherin	abcam	Cat#: ab33168	used at 1:100 dilution in 1% BSA, conjugated with Donkey anti-Rabbit secondary antibody, Alexa Fluor 647 (2µg/ml)

				and Alexa Fluor 488 (2µg/mL) in 1%BSA
antibody	Anti-Uroplakin3a	Santa Cruz	Cat#: sc-166808	used at 1:100 dilution in 1% BSA, conjugated with Donkey anti-Mouse secondary antibody, Alexa Fluor 647 (2µg/ml) in 1%BSA
antibody	Anti-CK1	Thermofisher	Cat#: MA1-06312	used at 1:100 dilution in 1% BSA, conjugated with Donkey anti-Mouse secondary antibody, Alexa Fluor 647 (2µg/ml) in 1%BSA
antibody	Anti-E-Cadherin	Thermofisher	Cat#: MA5-14408	used at 1:100 dilution in 1% BSA, conjugated with Donkey anti-Mouse secondary antibody, Alexa Fluor 647 (2µg/ml) in 1%BSA
antibody	Anti-ZO-1	abcam	Cat#: ab216880	used at 1:100 dilution in 1% BSA, conjugated with Donkey anti-Rabbit secondary antibody, Alexa Fluor 647 (2µg/ml) in 1%BSA
antibody	Anti-myeloperoxidase	abcam	Cat#: ab9535	used at 1:100 dilution in 1% BSA, conjugated with Donkey anti-Rabbit secondary antibody, Alexa Fluor 568 (2µg/ml) in 1%BSA
antibody	Anti-neutrophil elastase	abcam	Cat#: ab68672	used at 1:100 dilution in 1% BSA, conjugated with Donkey anti-Rabbit secondary antibody, Alexa Fluor 568 (2µg/ml) in 1%BSA
antibody	Anti-CD15	abcam	Cat#: ab665	used at 1:100 dilution in 1% BSA, conjugated with

				Donkey anti-Mouse secondary antibody, Alexa Fluor 568 (2µg/ml) in 1%BSA
antibody	Donkey anti-Mouse IgG (H+L) Highly Cross-Adsorbed Secondary Antibody, Alexa Fluor 647	Thermofisher	Cat#: A-31571	2 mg/ml
antibody	Donkey anti-Rabbit IgG (H+L) Highly Cross-Adsorbed Secondary Antibody, Alexa Fluor 647	Thermofisher	Cat#: A-31573	2 mg/ml
antibody	Goat anti-Mouse IgG (H+L) Highly Cross-Adsorbed Secondary Antibody, Alexa Fluor 488	Thermofisher	Cat#: A-11029	2 mg/ml
antibody	Donkey anti-Rabbit IgG (H+L) Highly Cross-Adsorbed Secondary Antibody, Alexa Fluor 568	Thermofisher	Cat#: A10042	2 mg/ml
antibody	Donkey anti-Mouse IgG (H+L) Highly Cross-Adsorbed Secondary Antibody, Alexa Fluor 568	Thermofisher	Cat#: A10037	2 mg/ml
peptide, recombinant protein	Fibronectin from human plasma	Sigma-Aldrich	Cat#: F1056	
peptide, recombinant protein	Native Collagen, Bovine dermis	AteloCell	Cat#: IAC-50	5 mg/ml
peptide, recombinant protein	Human IL-1α, research grade	Miltenyi Biotec	Cat#:130-093-894	1 µg/ml
peptide, recombinant protein	Human IL-1β, research grade	Miltenyi Biotec	Cat#:130-093-895	1 µg/ml
peptide, recombinant protein	Human IL-6, research grade	Miltenyi Biotec	Cat#:130-093-929	1 µg/ml
peptide, recombinant protein	Human IL-8, research grade	Miltenyi Biotec	Cat#:130-122-354	1 µg/ml
commercial assay or kit	MACSxpress® Whole Blood Neutrophil Isolation Kit, human	Miltenyi Biotec	Cat#:130-104-434	
software, algorithm	Imaris 9.5.1	Bitplane		
other	Gas chamber for stages with k-frame insert (160x110mm) - magnetic model with sliding lid.	okolab	Cat#: H201-K-FRAME	
other	Custom holder for 24mm x 60mm coverslip	okolab	Cat#:1x24by60-M	
other	µ-Slide 8 Well	ibidi	Cat#:80826	

other	Masterflex PharMed tubing, 0.89mm ID, 100 ft	Cole-Palmer	Cat#:GZ-95709-26	
other	Masterflex® Transfer Tubing, Tygon® 0.76mm ID	Cole-Palmer	Cat#:GZ-06419-03	
other	1.30 x 0.75 x 10 mm metallic tubes	Unimed	Cat#:9084 / 200.010-A	
other	1.00/0.75 x 20mm metallic tubes	Unimed	Cat#:200.010-A	
other	Aladdin programmable pump	WPI	Cat#: PUMP-NE-1000	

Cell culture of human bladder epithelial and bladder endothelial cells

The HTB9 human bladder epithelial carcinoma cell line (procured from ATCC, 5637) was cultured in RPMI 1640 medium (ATCC 30-2001) supplemented with 10% Fetal Bovine Serum (FBS) as recommended by the supplier. Human Bladder Microvascular Endothelial cells (HMVEC-Bd) (procured from Lonza, CC-7016) were cultured in Lonza EGM-2 MV BulletKit (CC-4147, CC-3156) medium. Both the epithelial and endothelial cells were generally cultured in their respective medium supplemented with 1X Antibiotic-Antimycotic (ThermoFisher 15240062). Epithelial cells were passaged by detachment with 0.05% Trypsin (Gibco) at 37°C for 3-5 minutes followed by neutralization of trypsin with RPMI 1640 medium/10% FBS. Bladder endothelial cells were passaged and split as recommended by the supplier. The cells used in all the experiments were at ten passages or fewer. The cell lines were tested routinely for mycoplasma contamination during passaging.

UPEC culture for infection of bladder epithelial cells in the bladder-chip

Uropathogenic *Escherichia coli* (UPEC) strain CFT073 was originally isolated from a pyelonephritis patient (Mobley et al., 1990) and provided by Prof. H.L.T. Mobley, University of Michigan, USA. A derivative strain expressing yellow fluorescent protein (YFP) was generated

by electroporation of CFT073 with the episomal plasmid pZA32-YFP, as described earlier (Dhar et al., 2015) . To induce expression of type 1 pili, UPEC was grown in LB media containing 25 µg/ml chloramphenicol under non-shaking conditions at 37 ^{0}C for 2 days prior to the experiment, to achieve a stationary phase culture (OD_{600}=1.5 and corresponding to a concentration of 1.5 x 10^{9} bacteria/ml). The bacteria were diluted 10-fold to a final concentration of 1.5 x 10^{8} cells/ml) and resuspended in a solution of pooled human female urine (Golden West Diagnostics Catalogue OH2010-pH) diluted 10-fold in Phosphate Buffered Saline (PBS, Gibco).

Recapitulation of human bladder physiology in human bladder-on-a-chip device

Bladder-chip devices made of polydimethylsiloxane (PDMS) were purchased from Emulate (Boston, USA). The dimensions of the microfluidic device were as follows: width of the channels- 1000 µm, height of the upper channel- 1000 µm, lower channel – 250 µm). For extracellular matrix (ECM) coating, a coating solution consisting of the ER-1 compound (Emulate) dissolved in ER-2 solution at 0.5 mg/mL (Emulate) was introduced in both apical and vascular channels and the chips were subsequently activated by exposing the bladder-chip for 20 minutes under UV light. The channels were then rinsed with fresh coating solution and the protocol was repeated once. The channels of the bladder-chip were then washed thoroughly with PBS before incubation with an ECM solution of 150 µg/ml bovine collagen type I (AteloCell, Japan,) and 30 µg/ml fibronectin from human plasma (Sigma-Aldrich) in PBS buffered with 15 mM HEPES solution (Gibco Catalogue F2006) for 1-2 hours at 37°C as described previously (Thacker et al., 2020). If not used directly, coated chips were stored at 4°C and pre-activated before use by incubation for 30 minutes with the same ECM solution at 37°C. Three days before the day of the experiment, HMVEC-Bd cells were seeded into lower channel of the inverted

bladder-chip device at 0.5 million cells/ml. Two days before the experiment, HTB9 cells were seeded into upper channel at 5 million cells/ml. The bladder endothelial and bladder epithelial cells were seeded into the device three and two days before the experiment in their respective medium supplemented with the 1X Antibiotic-Antimycotic solution. The antibiotics were removed prior to the experiment.

Characterization and immunostaining of human bladder epithelial and human bladder epithelial cells in ibidi wells and human bladder-chip

Human bladder epithelial and bladder endothelial cells were cultured inside ibidi 8-wells for one day. The cells were subsequently fixed with 4% paraformaldehyde (PFA) for 1 hr at room temperature. Fixed cells were then washed three times with 200 µL of PBS to remove residues of PFA, permeabilized with 0.15 % Triton X-100 for 15 minutes; washed three times with 200 µL of PBS to remove residues of detergent and then incubated in a blocking solution of 1% BSA in PBS for 1 hr. The cells were then incubated with primary antibodies (Anti-EpCAM, Anti-PECAM1, Anti-CK7, Anti-CK8, Anti-VE-Cadherin, Anti-Uroplakin3a, Anti-CK1, Anti-E-Cadherin, Anti-ZO-1, Anti-myeloperoxidase, Anti-neutrophil elastase, Anti-CD15) at a dilution of 1:100 in an antibody incubation buffer comprising 1% BSA and 0.01% Triton-100 in PBS. The ibidi wells were subsequently washed three times with PBS for 10 minutes each. Incubation with secondary antibody (Donkey anti-Mouse Alexa Fluor 647, Donkey anti-Mouse Alexa Fluor 568, Goat anti-Mouse Alexa Fluor 488, Donkey anti-Rabbit Alexa Fluor 647, Donkey anti-Rabbit Alexa Fluor 568, Donkey anti-Rabbit Alexa Fluor 488) at a concentration of 2 µg/mL in antibody incubation buffer was subsequently performed for 1 hour at room temperature. Excess antibody was removed by washing three times with PBS for 10 minutes each. Cell nuclei were

stained with DAPI (5 µg/mL, Sigma) for 30 minutes. Ibidi 8-wells were washed three times to remove unbound DAPI. Cells were covered with appropriate volume of PBS until imaging. Cells were imaged with 63X oil objective on Leica SP8 confocal microscope. Images were deconvolved using SVI Huygens (Quality, 0.05; Iterations, 40).

For characterization of the cell types on-chip, human bladder-chips with co-culture of bladder epithelial and bladder endothelial cells were kept under pooled diluted urine and EBM2 medium using P200 pipette tips for 2 days prior to PFA fixation. The cells inside human bladder chip were then immunostained following the protocol described above. Images were acquired with Leica HC FLUOTAR 25X (NA 0.95) multi-immersion objective on Leica SP8 confocal microscope.

Characterization of strain-pressure curve in the bladder-chip model

Elveflow OB1 MK3 – Microfluidic flow control system was used to control the negative pressure applied to the human bladder-chip. The control system was connected to the compressed air line (6 bar) for the positive pressure and diaphragm vacuum pump (KNF Neuberger) for the negative pressure. A negative pressure (0 to -900 mbar) with step function of -100mbar was subsequently applied to the vacuum channels in the bladder-chip using a Pressure Controller (Elveflow OB1 pressure controller). For these experiments, both bladder epithelial and endothelial cells were seeded on the respective sides in the devices. This experiment was performed with the chip maintained on the stage of the microscope and a brightfield image was acquired at each step increase of -100mbar, on Leica SP8 confocal microscope. The PDMS inter-

pore-to-pore distance was measured for 14 pore-to-pore combinations at each input of negative pressure. Linear fitting was performed using GraphPad Prism (version 9).

Mimicking bladder filling and voiding cycle in human bladder-chip

The stretching of the human bladder-chip was done using the Elveflow OB1 MK3 – Microfluidic flow control system connected to the compressed air line (6 bar) for the positive pressure and diaphragm vacuum pump (KNF Neuberger) for the negative pressure. Human bladder-chip in the relaxed (*voided bladder*) state was slowly perturbed with a linear ramp function to reach a stretched (*filled bladder*) state over a period of 2 hr. This period corresponded to the *filling bladder* state in Figure 1D. Bladder-chip was kept under stretched (*filled bladder*) state over the subsequent 2 hours. Micturition or urination was recapitulated by rapidly reducing the applied strain on the bladder-chip from the stretched (*filled bladder*) state to relaxed (*voided bladder*) state over a period of 2 minutes. Subsequently, the bladder-chip was maintained with no negative pressure applied in the vacuum channel under relaxed (*voided bladder*) state from (4hr + 2min to 6hr). This 6-hour bladder filling and voiding cycle with a duty cycle of 6hr was repeated continuously for the rest of the experiment.

Experimental setup and imaging parameters for time lapse imaging for UPEC infection in the human bladder-chip devices

The bladder-chip device was connected to the syringe pumps via gas impermeable PharMed® tubing (inner diameter =0.89 mm, Cole palmer GZ-95809-26) along with longer transparent Tygon tubings (internal diameter of 0.76mm, Masterflex transfer tubing Cole palmer GZ-06419-

03). The Harmed® tubing was connected to the inlet and outlet of the bladder-chip with 1.30 x 0.75 x 10 mm metallic tubes (Unimed) and transparent tubing with 1.00/0.75 x 20mm metallic tubes (Unimed). The bladder-chip connected to external sources of flow was then mounted onto a 24 x 60 mm No. 1 glass coverslip for microscopy imaging. When required for stretching experiments, tubing was also connected to the stretching channels on either side of the main channel. The connected device was subsequently assembled inside a temperature-controlled microscope environmental chamber at 37°C supplemented with 5% CO_2 (OKO labs H201-K-Frame). Time-lapse imaging was conducted using a Leica HC FLUOTAR 25X (NA 0.95) multi-immersion objective within custom made environmental chamber set at 37°C for infusion with syringe pumps. Water was pumped to the ring around the water objective at 9 Hz with pumping duration of 9 seconds and pumping interval 30 minutes, controlled by SRS software (HRZ=9, VPP=95). The autofocus mode (best focus, steps =9, range = 30 µm) was used to maintain the optical focus on the apical side of the PDMS membrane. The experiments were monitored frequently to ensure that the optical focus was maintained, and the experiment was halted and restarted if the focus was lost.

To enable rapid 3-D imaging across multiple spatial locations on-chip, we utilized the capability of the white light laser on the Leica SP8 confocal microscope to image at multiple wavelengths simultaneously. The excitation wavelengths were grouped into two sequences to minimize the spectral overlap. In the first sequence, laser emission at 555 nm was used to excite the Calmest Orange stain in the bladder epithelial cells. In the second laser excitation sequence, laser emission at 500 nm and 630 nm were used to excite the YFP within the bacteria and the cytoplasmic CellTracker^{TM} Deep Red in the human neutrophils. Images were acquired with a scan speed of 400-700 Hz and a zoom factor of 2.25 (206.67 µm x 206.67 µm) resulting in an

XY resolution of 450 nm depending on the number of pixels acquired per field of view. Z-stacks were acquired with 1 µm step sizes. Time lapse images were acquired with interval duration of ca. 15-17 minutes, in a subset of experiments this was further reduced to 7.5 minutes by imaging with the second sequence only at a z-step size of 2 µm.

Time lapse imaging for UPEC infections in the human bladder-chip devices

Pre-infection stage

The time-course of the entire experimental protocol is shown in a schematic in Figure 1. The bladder-chip device was perfused with diluted urine in the apical channel and EBM Endothelium phenol-red free medium supplemented with EGM-2 endothelial SingleQuots kit in the vascular channel. Prior to the commencement of infection, the chip was maintained at homeostasis and the epithelial cells were imaged for a period of two hours.

Infection stage

Stationary phase UPEC in diluted pooled urine at a concentration of 150 million cells/mL were flowed through the apical channel of the device at 1200 µL/hour for 1.5 hours. During this period, EBM2 media was flowed through the endothelial channel at 600 µL/hour.

Bacterial washout and neutrophil introduction stage

Next, the syringe connected to the apical channel was replaced with a fresh syringe containing pooled diluted urine, this solution was then flowed in the apical channel over the epithelial layer of the chip at a flow rate of 600 μL/hour over the next 3 hours. This allowed for the continuous removal of extracellular planktonic bacteria in the apical channel. At the same time, human neutrophils were introduced into the endothelial channel of the bladder-chip via flow. A solution of human neutrophils at a density of 2 million cells/mL isolated via negative selection was flowed through the vascular channel for 2 hours in EBM2 medium with at higher shear stress of η=1.0 dyne/cm^2 to enhance neutrophil attachment to endothelial cells.

<u>Neutrophil diapedesis stage</u>

Diapedesis of human neutrophils to epithelial side and subsequent interactions of neutrophils with UPEC was observed for the subsequent 3 hours since introduction of neutrophils into the vasculature side of the chip. During this period, the flow rate in the apical and vascular channels were maintained at 600 μL/hr and 3000 μL/hr respectively. During this period, in a subset of experiments, only the channels that were part of the second laser scanning sequence were imaged. Images of the CellTracker Orange dye for epithelial cell identification were not acquired (first laser scanning sequence). This enabled a number of fields of view to be captured with an enhanced temporal resolution and a frame rate of up to 7.5 minutes. For experiments studying the formation of NETs, the experiment was halted at this stage and the infected chips were fixed, permeabilized, blocked, and immunostained with anti-myeloperoxidase (abcam) or anti-neutrophil elastase (abcam) using the procedure described earlier. For all other experiments, live

imaging continued to the subsequent antibiotic treatment phase, Immunofluorescence for anti-myeloperoxidase and anti-neutrophil elastase was done as the procedure described previously.

Antibiotic treatment and growth cycles

Thereafter, syringes connected to both apical and vascular channels were changed and ampicillin at 250 µg/mL (used at ~40-fold over the minimum inhibitory concentration (MIC) of ampicillin against UPEC grown in EBM2 medium) was introduced in the diluted urine and the EBM2 media perfused into the apical and vascular channels, respectively, for 3 hours at a flow rate of 600 µl/hour. This was the first ampicillin treatment cycle; whose purpose was to eliminate extracellular bacteria in the apical channel and allow intracellular bacterial colonies (IBCs) to be identified. The medium was subsequently switched with antibiotic-free medium for next 8 hours to allow for IBC growth within epithelial cells. During this period, the flow within the apical channel was maintained, to remove bacteria that grew extracellularly either because they survived the antibiotic treatment or that were released from infected epithelial cells. The ampicillin and growth cycle were then repeated, to allow the assessment of the response of bacteria within IBCs to antibiotic treatment as well as characterize the subsequent regrowth.

Image analysis of confocal live-cell images

Image analysis was performed with Bitplane Imaris 9.5.1. The time-lapse imaging stack included five channels: uroepithelial cells (epithelial channel), transmitted light (bright field channel), UPEC (bacterial channel), neutrophils (neutrophil channel), and transmitted light (bright field

channel). Neutrophils were identified via the spot detection algorithm in Imaris used on the images from the neutrophil channel with the following parameters (Size, 8 µm; Quality, 4 to 8). Swarms of neutrophils generate dense aggregates that are ill-suited to quantification with the spot detection algorithm. To quantify the size of the swarms, we therefore segmented images in the neutrophil channel to generate surfaces via the automatic segmentation tool in Imaris. with the following parameters (Threshold, 10; Smooth Surfaces Detail, 0.5 or 1.0 µm). Unfortunately, the time resolution was insufficient to track individual neutrophils over time particularly since neutrophils formed small clumps and rapidly changed their cell shapes.

For UPEC volume inside IBCs, necessary 3D volume was cropped in Imaris to ease image analysis. Total bacterial volume inside IBC was detected by creating the surface (Threshold, 15; Smooth Surfaces Detail, 0.5 or 1 µm) on UPEC channel.

In cases of measuring extracellular UPEC growth, surface was generated (Threshold, 15; Smooth Surfaces Detail, 0.5 or 1 µm) on UPEC channel to calculate total extracellular volume in the field of view.

Infection experiments with relaxed and pre-stretched bladder chip

Human bladder-chip was kept in stretching state (ca. 10 % strain) for 2hr using Elveflow OB1 microfluidic control system. Post attainment of the stretched state, 200 µL of UPEC inoculum (150 million cells per mL) was introduced into the apical channel with 200 µL tips. During this period, EBM2 medium was maintained under static culture conditions. UPEC infection and attachment to the epithelial layer was then performed as described earlier during the stretched state. Subsequently, the pre-stretched bladder-chip was brought to relaxed state (0% strain) within 2 minutes. The bladder-chip was then incubated with Gentamicin (100 µg/ml) for 3 hours

introduced both on the apical and vascular channels of the bladder-chip to prevent extracellular growth. Similarly, a bladder-chip without any stretch applied to the membrane was also infected and processed as above. The bladder-chip was then washed three times with PBS, fixed, permeabilized, and then stained with the HCS Cell Mask ™ Deep red and imaged on a Leica SP8 confocal microscope. Bacterial surfaces were generated in Imaris (Threshold, 15; Smooth Surfaces Detail, 1.0 or 2.0 µm).

Isolation and Labelling of human neutrophils from fresh peripheral human blood

Primary human neutrophils were isolated via negative depletion method from human peripheral blood with MACSxpress® Whole Blood Neutrophil Isolation Kit (Miltenyi Biotec), following the manufacturers instructions. Isolation was performed without the use of a density-based centrifugation method. Isolated human neutrophils were then incubated with a 1µM solution CellTracker™ Deep Red in a serum free RPMI phenol red free medium for 30 minutes in a cell culture incubator maintained at 37 C and 5% CO_2 Labelled human neutrophils were then washed with 10ml of 20% FBS in RPMI phenol red free medium twice to remove the unbound dye. The human neutrophils were suspended in Lonza EBM2 medium at a cell density of 1 million cells/ml. In some instances, labelled human neutrophils were passed through a filter with 40 µm pores (Thermofisher) to remove neutrophil clusters that may have formed during the isolation process.

Scanning electron microscopy of human bladder-chip

UPEC were allowed to grow inside UPEC-infected epithelial cells in human bladder-chip was allowed for 6 hours (14 hr from start of UPEC infection) during the IBC 1st growth cycle. After 6 hours, human bladder-chip was fixed at room temperature for 1 hr with a mix of 1%

glutaraldehyde and 2% paraformaldehyde in 0.1 M phosphate buffer (pH 7.4). The fixed bladder-chip was kept in the fixative overnight (at 4°C). Post overnight fixation, human bladder-chip was cut open from the apical channel side. A scalpel was used to cut approximately in the middle of the apical channel side (height-1mm) to expose the bladder epithelial cells. The fixed chip was further fixed for 30 minutes in 1% osmium tetroxide in 0.1 M cacodylate buffer followed by washing with the distilled water. Next, the bladder-chip was dehydrated in a graded alcohol series and dried by passing them through the supercritical point of carbon dioxide (CPD300, Leica Microsystems). Finally, the bladder-chip was attached to an adhesive conductive surface followed by coating with a 3 – 4 nm layer of gold palladium metal (Quorum Q Plus, Quorum Technologies). Images of the cells were captured using a field emission scanning electron microscope (Merlin, Zeiss NTS).

In case of uninfected human bladder-chip (control), the human bladder chip was fixed at the same time point (14 hr from start of the experiment). For the case of NETs formed on epithelial layer, human bladder chip was fixed at 2 hours post neutrophil introduction into the endothelium side of the chip.

Preparation for transmission electron microscopy (TEM)

UPEC within infected human bladder-chips were allowed to proliferate for 6 hours (14 hr from start of UPEC infection) during the IBC 1st growth cycle. After 6 hours, human bladder-chip was fixed at room temperature for 1 hr with a mix of 1% glutaraldehyde and 2% paraformaldehyde in 0.1 M phosphate buffer (pH 7.4). The fixed bladder-chip was kept in the fixative overnight (at 4°C). Post overnight fixation, human bladder-chip was cut open from the apical channel side. A scalpel was used to cut approximately in the middle of the apical channel side (height-1mm) to expose the bladder epithelial cells. The bladder-chip was then washed in cacodylate buffer

(0.1M, pH 7.4), postfixed for 40 minutes in 1.0 % osmium tetroxide with 1.5% potassium ferrocyanide, and then fixed again with 1.0% osmium tetroxide alone. The bladder-chip was finally stained for 30 minutes in 1% uranyl acetate in water before being dehydrated through increasing concentrations of alcohol and then embedded in Durcupan ACM (Fluka, Switzerland) resin. The bladder-chip was then placed in Petri dishes so that approximately 1 mm of resin remained above the cells, and the dish than left in an oven at 65°C for 24 hours. Regions on interest, and corresponding to structures imaged with light microscopy were trimmed from the rest of the device, once the resin had hardened, and thin, 50 nm-thick sections were cut with a diamond knife, and collected onto single-slot copper grids with a pioloform support film. These were contrasted with lead citrate and uranyl acetate, and images taken with a transmission electron microscope at 80 kV (Tecnai Spirit, FEI Company with Eagle CCD camera).

Data availability statement

The datasets generated during and analysed during the current study are available from the corresponding authors on reasonable request and will be uploaded to Zenodo prior to publication.

Bibliography

Abraham, S.N., and Miao, Y. (2015). The nature of immune responses to urinary tract infections. Nat Rev Immunol *15*, 655–663.

Agace, W.W., Hedges, S.R., Ceska, M., and Svanborg, C. (1993). Interleukin-8 and the neutrophil response to mucosal gram-negative infection. J Clin Invest *92*, 780–785.

Agace, W.W., Patarroyo, M., Svensson, M., Carlemalm, E., and Svanborg, C. (1995). Escherichia coli induces transuroepithelial neutrophil migration by an intercellular adhesion molecule-1-dependent mechanism. Infect Immun *63*, 4054–4062.

Alon, R., Hammer, D.A., and Springer, T.A. (1995). Lifetime of the P-selectin-carbohydrate bond and its response to tensile force in hydrodynamic flow. Nature *374*, 539–542.

Andersen, T.E., Khandige, S., Madelung, M., Brewer, J., Kolmos, H.J., and Møller-Jensen, J. (2012). Escherichia coli uropathogenesis in vitro: invasion, cellular escape, and secondary infection analyzed in a human bladder cell infection model. Infect Immun *80*, 1858–1867.

Anderson, G.G., Palermo, J.J., Schilling, J.D., Roth, R., Heuser, J., and Hultgren, S.J. (2003). Intracellular Bacterial Biofilm-Like Pods in Urinary Tract Infections. Science *301*, 105–107.

Apodaca, G. (2004). The Uroepithelium: Not Just a Passive Barrier. Traffic *5*, 117–128.

Benam, K.H., Villenave, R., Lucchesi, C., Varone, A., Hubeau, C., Lee, H.-H., Alves, S.E., Salmon, M., Ferrante, T.C., Weaver, J.C., et al. (2016). Small airway-on-a-chip enables analysis of human lung inflammation and drug responses in vitro. Nat Methods *13*, 151–157.

Blango, M.G., and Mulvey, M.A. (2010). Persistence of Uropathogenic Escherichia coli in the Face of Multiple Antibiotics . Antimicrob Agents Ch *54*, 1855–1863.

Branzk, N., Lubojemska, A., Hardison, S.E., Wang, Q., Gutierrez, M.G., Brown, G.D., and Papayannopoulos, V. (2014). Neutrophils sense microbe size and selectively release neutrophil extracellular traps in response to large pathogens. Nat Immunol *15*, 1017–1025.

Brinkmann, V., Reichard, U., Goosmann, C., Fauler, B., Uhlemann, Y., Weiss, D.S., Weinrauch, Y., and Zychlinsky, A. (2004). Neutrophil Extracellular Traps Kill Bacteria. Science *303*, 1532–1535.

Bryskier, A. (2020). Antimicrobial Agents: Antibacterials and Antifungals. pp. 113–162.

Cakir, B., Xiang, Y., Tanaka, Y., Kural, M.H., Parent, M., Kang, Y.-J., Chapeton, K., Patterson, B., Yuan, Y., He, C.-S., et al. (2019). Engineering of human brain organoids with a functional vascular-like system. Nat Methods *16*, 1169–1175.

Carattino, M.D., Prakasam, H.S., Ruiz, W.G., Clayton, D.R., McGuire, M., Gallo, L.I., and Apodaca, G. (2013). Bladder filling and voiding affect umbrella cell tight junction organization and function. Am J Physiol-Renal *305*, F1158–F1168.

Clevers, H. (2016). Modeling Development and Disease with Organoids. Cell *165*, 1586–1597.

Duncan, M.J., Li, G., Shin, J.-S., Carson, J.L., and Abraham, S.N. (2004). Bacterial Penetration of Bladder Epithelium through Lipid Rafts. J Biol Chem *279*, 18944–18951.

Ermert, D., Urban, C.F., Laube, B., Goosmann, C., Zychlinsky, A., and Brinkmann, V. (2009). Mouse Neutrophil Extracellular Traps in Microbial Infections. J Innate Immun *1*, 181–193.

Foxman, B. (2010). The epidemiology of urinary tract infection. Nat Rev Urol *7*, 653–660.

Gloeckner, D.C., SACKS, M.S., FRASER, M.O., SOMOGYI, G.T., GROAT, W.C. de, and CHANCELLOR, M.B. (2002). Passive Biaxial Mechanical Properties of the Rat Bladder Wall After Spinal Cord Injury. J Urology *167*, 2247–2252.

Grassart, A., Malardé, V., Gobba, S., Sartori-Rupp, A., Kerns, J., Karalis, K., Marteyn, B., Sansonetti, P., and Sauvonnet, N. (2019). Bioengineered Human Organ-on-Chip Reveals Intestinal Microenvironment and Mechanical Forces Impacting Shigella Infection. Cell Host Microbe *26*, 435-444.e4.

Hannan, T.J., Totsika, M., Mansfield, K.J., Moore, K.H., Schembri, M.A., and Hultgren, S.J. (2012). Host–pathogen checkpoints and population bottlenecks in persistent and intracellular uropathogenic Escherichia coli bladder infection. Fems Microbiol Rev *36*, 616–648.

Haraoka, M., Hang, L., Frendéus, B., Godaly, G., Burdick, M., Strieter, R., and Svanborg, C. (1999). Neutrophil Recruitment and Resistance to Urinary Tract Infection. J Infect Dis *180*, 1220–1229.

Hedges, S., Svensson, M., and Svanborg, C. (1992). Interleukin-6 response of epithelial cell lines to bacterial stimulation in vitro. Infect Immun *60*, 1295–1301.

Horsley, H., Dharmasena, D., Malone-Lee, J., and Rohn, J.L. (2018). A urine-dependent human urothelial organoid offers a potential alternative to rodent models of infection. Sci Rep-Uk *8*, 1238.

Hsieh, M.M., Everhart, J.E., Byrd-Holt, D.D., Tisdale, J.F., and Rodgers, G.P. (2007). Prevalence of Neutropenia in the U.S. Population: Age, Sex, Smoking Status, and Ethnic Differences. Ann Intern Med *146*, 486.

Huh, D., Matthews, B.D., Mammoto, A., Montoya-Zavala, M., Hsin, H.Y., and Ingber, D.E. (2010a). Reconstituting Organ-Level Lung Functions on a Chip. Science *328*, 1662–1668.

Huh, D., Matthews, B.D., Mammoto, A., Montoya-Zavala, M., Hsin, H.Y., and Ingber, D.E. (2010b). Reconstituting Organ-Level Lung Functions on a Chip. Science *328*, 1662–1668.

Hung, C.-S., Dodson, K.W., and Hultgren, S.J. (2009). A murine model of urinary tract infection. Nat Protoc *4*, 1230–1243.

Hunstad, D.A., and Justice, S.S. (2010). Intracellular Lifestyles and Immune Evasion Strategies of Uropathogenic Escherichia coli. Annu Rev Microbiol *64*, 203–221.

Iosifidis, G., and Duggin, I.G. (2020). Distinct Morphological Fates of Uropathogenic Escherichia coli Intracellular Bacterial Communities: Dependency on Urine Composition and pH. Infect Immun *88*.

Jalili-Firoozinezhad, S., Gazzaniga, F.S., Calamari, E.L., Camacho, D.M., Fadel, C.W., Bein, A., Swenor, B., Nestor, B., Cronce, M.J., Tovaglieri, A., et al. (2019). A complex human gut microbiome cultured in an anaerobic intestine-on-a-chip. Nat Biomed Eng *3*, 520–531.

Jang, K.-J., Mehr, A.P., Hamilton, G.A., McPartlin, L.A., Chung, S., Suh, K.-Y., and Ingber, D.E. (2013). Human kidney proximal tubule-on-a-chip for drug transport and nephrotoxicity assessment. Integr Biol *5*, 1119–1129.

Jang, K.-J., Otieno, M.A., Ronxhi, J., Lim, H.-K., Ewart, L., Kodella, K.R., Petropolis, D.B., Kulkarni, G., Rubins, J.E., Conegliano, D., et al. (2019). Reproducing human and cross-species drug toxicities using a Liver-Chip. Sci Transl Med *11*, eaax5516.

Justice, S.S., Hung, C., Theriot, J.A., Fletcher, D.A., Anderson, G.G., Footer, M.J., and Hultgren, S.J. (2004). Differentiation and developmental pathways of uropathogenic Escherichia coli in urinary tract pathogenesis. Proc National Acad Sci *101*, 1333–1338.

Kang, Y.B. (Abraham), Rawat, S., Duchemin, N., Bouchard, M., and Noh, M. (2017). Human Liver Sinusoid on a Chip for Hepatitis B Virus Replication Study. Micromachines-Basel *8*, 27.

Kienle, K., and Lämmermann, T. (2016). Neutrophil swarming: an essential process of the neutrophil tissue response. Immunol Rev *273*, 76–93.

Kim, H.J., and Ingber, D.E. (2013). Gut-on-a-Chip microenvironment induces human intestinal cells to undergo villus differentiation. Integr Biol *5*, 1130–1140.

Kim, H.J., Li, H., Collins, J.J., and Ingber, D.E. (2016). Contributions of microbiome and mechanical deformation to intestinal bacterial overgrowth and inflammation in a human gut-on-a-chip. Proc National Acad Sci *113*, E7–E15.

Klein, R.D., and Hultgren, S.J. (2020). Urinary tract infections: microbial pathogenesis, host-pathogen interactions and new treatment strategies. Nat Rev Microbiol *18*, 211–226.

Korkmaz, I., and Rogg, B. (2007). A simple fluid-mechanical model for the prediction of the stress–strain relation of the male urinary bladder. J Biomech *40*, 663–668.

Kreisel, D., Nava, R.G., Li, W., Zinselmeyer, B.H., Wang, B., Lai, J., Pless, R., Gelman, A.E., Krupnick, A.S., and Miller, M.J. (2010). In vivo two-photon imaging reveals monocyte-dependent neutrophil extravasation during pulmonary inflammation. Proc National Acad Sci *107*, 18073–18078.

Lämmermann, T., Afonso, P.V., Angermann, B.R., Wang, J.M., Kastenmüller, W., Parent, C.A., and Germain, R.N. (2013). Neutrophil swarms require LTB4 and integrins at sites of cell death in vivo. Nature *498*, 371–375.

Ley, K., Laudanna, C., Cybulsky, M.I., and Nourshargh, S. (2007). Getting to the site of inflammation: the leukocyte adhesion cascade updated. Nat Rev Immunol *7*, 678–689.

Martinez, J.J., Mulvey, M.A., Schilling, J.D., Pinkner, J.S., and Hultgren, S.J. (2000). Type 1 pilus-mediated bacterial invasion of bladder epithelial cells. Embo J *19*, 2803–2812.

Metzler, K.D., Fuchs, T.A., Nauseef, W.M., Reumaux, D., Roesler, J., Schulze, I., Wahn, V., Papayannopoulos, V., and Zychlinsky, A. (2011). Myeloperoxidase is required for neutrophil extracellular trap formation: implications for innate immunity. Blood *117*, 953–959.

Mulvey, M.A., Lopez-Boado, Y.S., Wilson, C.L., Roth, R., Parks, W.C., Heuser, J., and Hultgren, S.J. (1998). Induction and Evasion of Host Defenses by Type 1-Piliated Uropathogenic Escherichia coli. Science *282*, 1494–1497.

Mysorekar, I.U., and Hultgren, S.J. (2006). Mechanisms of uropathogenic Escherichia coli persistence and eradication from the urinary tract. Proc National Acad Sci *103*, 14170–14175.

Nagamatsu, K., Hannan, T.J., Guest, R.L., Kostakioti, M., Hadjifrangiskou, M., Binkley, J., Dodson, K., Raivio, T.L., and Hultgren, S.J. (2015). Dysregulation of Escherichia coli α-hemolysin expression alters the course of acute and persistent urinary tract infection. Proc National Acad Sci *112*, E871–E880.

Nawroth, J.C., Lucchesi, C., Cheng, D., Shukla, A., Ngyuen, J., Shroff, T., Varone, A., Karalis, K., Lee, H.-H., Alves, S., et al. (2020). A Microengineered Airway Lung Chip Models Key Features of Viral-induced Exacerbation of Asthma. Am J Resp Cell Mol *63*, 591–600.

Nourshargh, S., Hordijk, P.L., and Sixt, M. (2010). Breaching multiple barriers: leukocyte motility through venular walls and the interstitium. Nat Rev Mol Cell Bio *11*, 366–378.

Novak, R., Ingram, M., Marquez, S., Das, D., Delahanty, A., Herland, A., Maoz, B.M., Jeanty, S.S.F., Somayaji, M.R., Burt, M., et al. (2020). Robotic fluidic coupling and interrogation of multiple vascularized organ chips. Nat Biomed Eng *4*, 407–420.

Oliveira, S. de, Rosowski, E.E., and Huttenlocher, A. (2016). Neutrophil migration in infection and wound repair: going forward in reverse. Nat Rev Immunol *16*, 378–391.

Papayannopoulos, V., Metzler, K.D., Hakkim, A., and Zychlinsky, A. (2010). Neutrophil elastase and myeloperoxidase regulate the formation of neutrophil extracellular traps. J Cell Biology *191*, 677–691.

Parekh, A., Cigan, A.D., Wognum, S., Heise, R.L., Chancellor, M.B., and Sacks, M.S. (2010). Ex vivo deformations of the urinary bladder wall during whole bladder filling: Contributions of extracellular matrix and smooth muscle. J Biomech *43*, 1708–1716.

Pascalis, R.D., Parnell, W.J., Abrahams, I.D., Shearer, T., Daly, D.M., and Grundy, D. (2018). The inflation of viscoelastic balloons and hollow viscera. Proc Royal Soc *474*, 20180102.

Putrinš, M., Kogermann, K., Lukk, E., Lippus, M., Varik, V., and Tenson, T. (2015). Phenotypic Heterogeneity Enables Uropathogenic Escherichia coli To Evade Killing by Antibiotics and Serum Complement. Infect Immun *83*, 1056–1067.

Robino, L., Scavone, P., Araujo, L., Algorta, G., Zunino, P., and Vignoli, R. (2013). Detection of intracellular bacterial communities in a child with Escherichia coli recurrent urinary tract infections. Pathog Dis *68*, 78–81.

Ronaldson-Bouchard, K., and Vunjak-Novakovic, G. (2018). Organs-on-a-Chip: A Fast Track for Engineered Human Tissues in Drug Development. Cell Stem Cell *22*, 310–324.

Rosen, D.A., Hooton, T.M., Stamm, W.E., Humphrey, P.A., and Hultgren, S.J. (2007). Detection of Intracellular Bacterial Communities in Human Urinary Tract Infection. Plos Med *4*, e329.

Rossi, G., Manfrin, A., and Lutolf, M.P. (2018). Progress and potential in organoid research. Nat Rev Genet *19*, 671–687.

Sato, T., Vries, R.G., Snippert, H.J., Wetering, M. van de, Barker, N., Stange, D.E., Es, J.H. van, Abo, A., Kujala, P., Peters, P.J., et al. (2009). Single Lgr5 stem cells build crypt-villus structures in vitro without a mesenchymal niche. Nature *459*, 262–265.

Scott, V.C.S., Haake, D.A., Churchill, B.M., Justice, S.S., and Kim, J.-H. (2015). Intracellular Bacterial Communities: A Potential Etiology for Chronic Lower Urinary Tract Symptoms. Urology *86*, 425–431.

Shah, P., Fritz, J.V., Glaab, E., Desai, M.S., Greenhalgh, K., Frachet, A., Niegowska, M., Estes, M., Jäger, C., Seguin-Devaux, C., et al. (2016). A microfluidics-based in vitro model of the gastrointestinal human–microbe interface. Nat Commun *7*, 11535.

Si, L., Bai, H., Rodas, M., Cao, W., Oh, C.Y., Jiang, A., Nurani, A., Zhu, D.Y., Goyal, G., Gilpin, S.E., et al. (2020). Human organs-on-chips as tools for repurposing approved drugs as potential influenza and COVID19 therapeutics in viral pandemics. Biorxiv 2020.04.13.039917.

Smith, Y.C., Grande, K.K., Rasmussen, S.B., and O'Brien, A.D. (2006). Novel Three-Dimensional Organoid Model for Evaluation of the Interaction of Uropathogenic Escherichia coli with Terminally Differentiated Human Urothelial Cells. Infect Immun *74*, 750–757.

Solis, A.G., Bielecki, P., Steach, H.R., Sharma, L., Harman, C.C.D., Yun, S., Zoete, M.R. de, Warnock, J.N., To, S.D.F., York, A.G., et al. (2019). Mechanosensation of cyclical force by PIEZO1 is essential for innate immunity. Nature *573*, 69–74.

Son, K., Mukherjee, M., McIntyre, B.A.S., Eguez, J.C., Radford, K., LaVigne, N., Ethier, C., Davoine, F., Janssen, L., Lacy, P., et al. (2017). Improved recovery of functionally active eosinophils and neutrophils using novel immunomagnetic technology. J Immunol Methods *449*, 44–55.

Song, J., Duncan, M.J., Li, G., Chan, C., Grady, R., Stapleton, A., and Abraham, S.N. (2007). A Novel TLR4-Mediated Signaling Pathway Leading to IL-6 Responses in Human Bladder Epithelial Cells. Plos Pathog *3*, e60.

Spaulding, C.N., Klein, R.D., Ruer, S., Kau, A.L., Schreiber, H.L., Cusumano, Z.T., Dodson, K.W., Pinkner, J.S., Fremont, D.H., Janetka, J.W., et al. (2017). Selective depletion of uropathogenic E. coli from the gut by a FimH antagonist. Nature *546*, 528–532.

Suzuki, K., Koyanagi-Aoi, M., Uehara, K., Hinata, N., Fujisawa, M., and Aoi, T. (2019). Directed differentiation of human induced pluripotent stem cells into mature stratified bladder urothelium. Sci Rep-Uk *9*, 10506.

Thacker, V.V., Sharma, K., Dhar, N., Mancini, G.-F., Sordet-Dessimoz, J., and McKinney, J.D. (2020a). Rapid endothelial infection, endothelialitis and vascular damage characterise SARS-CoV-2 infection in a human lung-on-chip model. Biorxiv 2020.08.10.243220.

Thacker, V.V., Dhar, N., Sharma, K., Barrile, R., Karalis, K., and McKinney, J.D. (2020b). A lung-on-chip model of early M. tuberculosis infection reveals an essential role for alveolar epithelial cells in controlling bacterial growth. Elife *9*, e59961.

Tovaglieri, A., Sontheimer-Phelps, A., Geirnaert, A., Prantil-Baun, R., Camacho, D.M., Chou, D.B., Jalili-Firoozinezhad, S., Wouters, T. de, Kasendra, M., Super, M., et al. (2019). Species-specific enhancement of enterohemorrhagic E. coli pathogenesis mediated by microbiome metabolites. Microbiome *7*, 43.

Truschel, S.T., Wang, E., Ruiz, W.G., Leung, S.-M., Rojas, R., Lavelle, J., Zeidel, M., Stoffer, D., and Apodaca, G. (2002). Stretch-regulated Exocytosis/Endocytosis in Bladder Umbrella Cells. Mol Biol Cell *13*, 830–846.

Wang, E.C.Y., Lee, J.-M., Ruiz, W.G., Balestreire, E.M., Bodungen, M. von, Barrick, S., Cockayne, D.A., Birder, L.A., and Apodaca, G. (2005). ATP and purinergic receptor–dependent membrane traffic in bladder umbrella cells. J Clin Invest *115*, 2412–2422.

Wang, J., Wang, C., Xu, N., Liu, Z.-F., Pang, D.-W., and Zhang, Z.-L. (2019). A virus-induced kidney disease model based on organ-on-a-chip: Pathogenesis exploration of virus-related renal dysfunctions. Biomaterials *219*, 119367.

Yu, Y., Kwon, K., Tsitrin, T., Bekele, S., Sikorski, P., Nelson, K.E., and Pieper, R. (2017). Characterization of Early-Phase Neutrophil Extracellular Traps in Urinary Tract Infections. Plos Pathog *13*, e1006151.

Zahler, S., Kowalski, C., Brosig, A., Kupatt, C., Becker, B.F., and Gerlach, E. (1997). The function of neutrophils isolated by a magnetic antibody cell separation technique is not altered in comparison to a density gradient centrifugation method. J Immunol Methods *200*, 173–179.

Zalewska-Piątek, B., Olszewski, M., Lipniacki, T., Błoński, S., Wieczór, M., Bruździak, P., Skwarska, A., Nowicki, B., Nowicki, S., and Piątek, R. (2020). A shear stress micromodel of urinary tract infection by the Escherichia coli producing Dr adhesin. Plos Pathog *16*, e1008247.

Zhou, M., Zhang, X., Wen, X., Wu, T., Wang, W., Yang, M., Wang, J., Fang, M., Lin, B., and Lin, H. (2016). Development of a Functional Glomerulus at the Organ Level on a Chip to Mimic Hypertensive Nephropathy. Sci Rep-Uk *6*, 31771.